THESIS FOR THE DEGREE OF DOCTOR OF PHILOSOPHY

Molecular-Level Insights into Next-Generation Battery Electrolytes

Mirna Alhanash

Department of Physics

CHALMERS UNIVERSITY OF TECHNOLOGY

Gothenburg, Sweden 2025

Molecular-Level Insights into Next-Generation Battery Electrolytes

Mirna Alhanash

ISBN 978-91-8103-293-2

Doktorsavhandlingar vid Chalmers tekniska högskola
Ny serie nr 5751
ISSN 0346-7185751
https://doi.org/10.63959/chalmers.dt/5751

Department of Physics
Chalmers University of Technology
SE-412 96 Gothenburg
Sweden
Telephone + 46 (0)31-772 1000

Cover:

Cover art by Ziad Alhanash, depicting computational research as the seed from which future, world-powering batteries grow.

Chalmers Digitaltryck

Gothenburg, Sweden 2025

Molecular-Level Insights into Next-Generation Battery Electrolytes

Mirna Alhanash

Department of Physics

Chalmers University of Technology

Abstract

Unconventional electrolytes, especially highly concentrated electrolytes (HCEs) and deep eutectic electrolytes (DEEs), are emerging as promising candidates for a wide range of battery chemistries, including lithium-ion, lithium metal, and calcium batteries. Their tunability, non-volatility, and wide electrochemical stability windows make them attractive alternatives to conventional electrolytes. However, while the fundamental properties that make HCEs and DEEs attractive, such as their electrochemical stability and low melting points, are driven by molecular interactions, the interplay between these interactions and local structuring and their effects on macroscopic properties remains poorly understood.

To bridge this gap, we employ tight-binding and classical molecular dynamics simulations to investigate the local coordination environment, hydrogen bonding networks, and molecular-level ordering, especially in DEEs. By focusing on the interplay between hydrogen bond donors and different anion sizes and symmetries in hydrogen bond acceptors, we systematically explore how molecular interactions influence solvation structure and ion mobility. Our findings suggest that anion symmetry and size, together with hydrogen bonding strength, govern the solvation shell dynamics and overall diffusion behavior, impacting macroscopic transport properties.

Understanding these molecular-scale mechanisms is key to optimizing DEE formulations for different battery chemistries. This work provides fundamental insights into the structure and property relationships of DEEs, enabling their rational design for safer, more efficient energy storage technologies.

Keywords: tight-binding, deep eutectic solvent, deep eutectic electrolyte, xTB, molecular dynamics, electrolyte, local structure, multivalent, heterogeneity.

List of Papers

This thesis is based on the work contained in the following papers:

I Molecular-Level Heterogeneity in Deep Eutectic Electrolytes
M. Alhanash, C. Cruz, and P. Johansson.
Phys. Chem. Chem. Phys, 2025. DOI:10.1039/d5cp01828e.

II Molecular Insights into Calcium-Based Deep Eutectic Electrolytes for Next-Generation Batteries
M. Alhanash, C. Cruz, and P. Johansson
In manuscript.

III Liquid Electrolytes for Multivalent Batteries in Roadmap on Molecular Modelling of Electrochemical Energy Materials
T. Mandai, T. Hosaka, M. Alhanash, and P. Johansson
Journal of Physics: Energy, 2023, 5(4), 22-24. DOI:10.1088/2515-7655/acfe9b

IV Urea-based Ternary Deep Eutectic Electrolytes for Lithium Metal Battery
Nanako Ito, Tomooki Hosaka, Mirna Alhanash, Ryoichi Tatara, Zachary T. Gossage, Patrik Johansson, and Shinichi Komaba
Submitted, under review.

V NaTFSI- Adiponitrile Highly Concentrated Electrolytes for Na-Ion and Na-O2 Batteries
C. J. Franko, B. L. Pinto, O. Velenosi, M. Alhanash, F. Åren, C.H. Yim, P. Johansson, Y. Abu-Lebdeh, and G. R. Goward
Journal of Physical Chemistry C, 2025, 129(20), 9259-9270. DOI:10.1021/acs.jpcc.4c07934.

Contribution Report

I. I performed the semi-empirical simulations, analyzed the data, and was primarily responsible for writing the manuscript.

II. I performed the computations, analyzed the data, and was primarily responsible for writing the manuscript.

III. I contributed to the prospects of different liquid electrolytes part of the review.

IV. I performed the computational section of the study and contributed to the corresponding parts of the manuscript along with my co-authors.

V. I performed the computational section of the study and contributed to the corresponding parts of the manuscript along with my co-authors.

List of Abbreviations

ADF Angular distribution function

ADN Adiponitrile

AGG Aggregates

AIMD ab initio molecular dynamics

BF_4 Tetrafluoroborate

Bhfip Tetrakis(hexafluoroisopropyloxy)borate

BOB Bis(oxalato)borate

CDF Cumulative distribution function

ChCl Choline chloride

CIP Contact-ion pair

CN Coordination number

CNDO Complete neglect of differential overlap

DEE Deep eutectic electrolyte

DES Deep eutectic solvent

DFOB Difluoro(oxalato)borate

DFT Density functional theory

DFTB Density functional tight binding

ESW Electrochemical stability window

EV Electric vehicle

FF Force field

GWh Gigawatt-hour

HBA Hydrogen bond acceptor

HBD Hydrogen bond donor

HCE High-concentration electrolyte

HF Hartree-Fock

IL Ionic liquid

INDO Intermediate neglect of differential overlap

LCAO Linear combination of atomic orbitals

LHCE Localized high-concentration electrolyte

LIB Lithium-ion battery

MD Molecular dynamics

MLH Molecular-level heterogeneity

MO Molecular orbital

MSD Mean square displacement

NDDO Neglect of diatomic differential overlap

pCN Partial coordination number

pSN Partial solvation number

QM Quantum mechanics

RDF Radial distribution function

SDF Spatial distribution function

SEI Solid-electrolyte interphase

SN Solvation number

SQM Semi-empirical quantum mechanical method

TB Tight binding

TWh Terawatt-hour

U Urea

WFT wave function theory

xTB Extended tight binding

ZDO Zero-differential overlap

Prologue

"It is the theory that decides what we can observe."
Einstein cited by Heisenberg in "Physics and Beyond" 1971

Plato's Allegory of the Cave imagines an ascent from shadows into sunlight. Along that path, the divided line reminds us that mathematical reasoning sits between opinion and direct insight: useful, disciplined, and incomplete. Kant's caution in the Critique of Pure Reason reminds us: Measurement gives us phenomena (appearances), but reality in itself (noumenon) remains unknowable.

In this thesis, computational methods act as lenses with a focus on understanding materials at a molecular level, how local organisation and interactions give rise to what we later observe in bulk behaviour. This could help suggest how to design electrolytes for next-generation batteries, and, in time, help power an electrified world.

Methods are only as good as their use, and models are not the world. The pages that follow try to narrow the distance between shadow and source without claiming to stand in the sun

Table of Contents

Chapter 1

Introduction

As the world is moving towards mobility electrification, together with a steady increase in global energy consumption, there is an urgent and growing need for energy systems.[1,2] Battery energy storage systems are central to this transition; they do so by buffering the intermittency of renewables, stabilizing the grid, and powering electric vehicles (EVs).[3,4] Yet the extraction and processing of critical battery materials such as lithium, cobalt, and nickel raise environmental, geopolitical concerns, and logistical challenges, driving the search for alternative chemistries that combine high performance with more abundant, lower-cost raw materials.

Today, lithium-ion batteries (LIBs) dominate the market thanks to their high gravimetric energy density and mature manufacturing base, representing a significant leap from earlier battery models. However, McKinsey projects that the global demand for LIBs in the coming decade is expected to experience a significant spike.[1] The needed GWh (gigawatt-hour) capacity is expected to grow from approximately 700 GWh in 2022 to an estimated 4.7 TWh (terawatt-hour) by 2030, with a market value of more than $400 billion.

Notably, a substantial portion of this demand, around 4,300 GWh, will be driven by batteries for mobility applications, particularly EVs, in response to the rapid growth of the mobility sector. BESS is anticipated to have a compound annual growth rate (CAGR) of 30 percent. The demand for GWh (gigawatt-hours) of energy to support these applications in 2030 is anticipated to be on par with the current total GWh required for all applications, such as portable electronics (e.g., smartphones, laptops) and renewable energy storage.

As LIBs approach intrinsic limits in energy density and resource availability, metal-anode systems, most notably lithium metal and emerging multivalent chemistries like calcium, have captured intense research interest.[5–9] These “next-generation” batteries

promise even higher specific capacities and, in the case of calcium, the benefit of earth-abundant, low-cost raw materials.

A battery's electrolyte plays an instrumental role in battery performance, governing ion transport, electrochemical stability, and safety. Conventional carbonate-based solvents sometimes struggle with dendrite formation on reactive metal anodes and volatility.[10,11] In contrast, unconventional electrolytes such as highly concentrated electrolytes (HCEs) (**Paper V**) and deep eutectic electrolytes (DEEs) (**Paper I** and **II**) have attracted significant research attention due to their multifaceted properties that could mitigate these challenges. They can widen stability windows, modulate solvation structures, and avoid side reactions. [12–14] DEEs in particular offer a spectrum of desirable characteristics, including tunability, wide electrochemical stability windows, and low vapor pressures, rendering them attractive for both lithium and emerging calcium electrolytes. They hold the potential to enhance safety and optimize the performance of energy storage systems. Therefore, exploring DEEs as battery electrolytes has become an active research area aimed at harnessing their unique properties for next-generation energy storage solutions.

Computational simulations, which are guided by fundamental theories like Density Functional Theory (DFT), have become crucial tools to aid in the discovery of novel and optimized materials. At the atomic level, these simulations employ quantum mechanics to calculate electronic structures, bonding, and energies, enabling precise predictions of material behavior under diverse conditions. However, solving the Schrödinger equation becomes computationally expensive for larger systems, leading to the use of Newtonian simulations. Molecular dynamics (MD) techniques offer insights into the stability, reactivity, and responses of complex structures. Although the combined technique AIMD simulations provide high accuracy, their computational demands limit system size and time scales, despite notable progress in the field. One way to bridge the gap between AIMD and classical MD is the use of semi-empirical quantum mechanical (SQM) methods, such as tight-binding theory (TB), which attempts to balance computational time and accuracy [15]. These SQM methods are typically built upon a minimal basis self-consistent field approach focused on valence electrons, which originates from either Hartree-Fock theory or Kohn-Sham DFT, which will be discussed further in Chapter 4.

The relevance of computer simulations in materials research cannot be overstated. Therefore, these computational approaches are vital in the pursuit of new materials for different applications, from advanced electronics and renewable materials to pharmaceuticals and catalysis.[35,57] They offer a cost-effective and time-efficient way to

explore a vast chemical space, identifying promising candidates with specific properties and functionalities before investing resources in experimental work. When complemented with experimental analysis, they collectively paint a wider, more reliable picture, enabling deeper understanding and more advanced materials design.

The utilization of MD simulations in materials discovery encompasses various computational approaches and software tools. In **Papers I, II, and IV**, the tight-binding theory xTB, implemented through CP2K, is utilized. The latter is a semi-empirical quantum mechanical method with an extended tight-binding framework and is used for quantum mechanical calculations of electronic structure and properties. Within this framework, we investigate salts with distinct anion geometries for potential use in DEEs for lithium batteries in **Paper I** and for calcium-based batteries in **Paper II**. Conversely, in **paper V**, MD simulations for sodium battery electrolytes are generated using MOPAC, which employs an SQM method. **Paper III** delves into the prospects and constraints associated with liquid electrolytes like DEEs.

By integrating, semi-empirical tight-binding (xTB) method for detailed local structure insights and classical MD for longer timescale transport, this work illuminates how molecular interactions guide electrolyte design. The findings pave the way toward understanding DEEs at a molecular level and their potential use in sustainable, high-performance batteries that leverage earth-abundant materials and informed molecular tuning.

1.1. Scope of Thesis

This thesis investigates a range of unconventional liquid electrolytes, such as HCEs and DEEs, for LIBs and next-generation chemistries, via MD simulations grounded in SQM methods. In order to connect microscopic insights to macroscopic performance, we introduce a multi-metric analysis pipeline including radial distribution functions, coordination numbers, spatial distribution functions, hydrogen-bond profiling, and a molecular-level heterogeneity (MLH) index, which highlights local structure and dynamical properties of DEEs.

The work is structured around five papers. In **Paper I**, lithium–NMA DEEs composed of N-methyl-acetamide and three lithium salts with distinct anion geometries are simulated to study hydrogen-bond distributions, introduce a molecular-level heterogeneity metric, and reveal the influence of anion symmetry and size on coordination shells and local structure. **Paper II** extends this framework to calcium–

NMA DEEs, highlighting the effect of using a divalent cation on coordination numbers and hydrogen-bond networks. **Paper III** provides a prospect of modeling liquid electrolytes and their future use in multivalent systems. In **Paper IV**, xTB simulations of urea-based DESs at varying concentrations uncover concentration and solvent-dependent shifts in lithium coordination and hydrogen-bond patterns. Finally, **Paper V** explores the local structure and concentration variation of NaTFSI–Adiponitrile as a highly concentrated electrolyte for Na-Ion and Na-O_2 Batteries. Using the trajectories from MOPAC, we calculated the (partial) coordination and solvation numbers of the cations in the different lithium and sodium systems. Together, these studies deepen our understanding of emerging battery electrolytes at the molecular level and demonstrate the utility of semi-empirical methods for probing interactions and ordering that guide electrolyte design.

1.2. Limitations

This thesis focuses on computational modelling, mainly using semi-empirical MD methods to investigate structural and dynamic analyses. It therefore does not include experiments nor cover interfacial phenomena like solid–electrolyte interphase formation. While the xTB method used for semi-empirical MDs offers a fair tradeoff between accuracy and speed, the chosen time scale of about 90-100 ps does not show diffusivity information since time scales closer to 50–100 ns resolve diffusive onset. Thus, we rely on classical MD for transport calculations, even though xTB, when paired with enhanced sampling or other techniques, could potentially access the diffusive regime. Finally, although next-generation electrolytes such as calcium-based systems are often promoted as sustainable and low-cost due to calcium's abundance, this thesis does not include a life-cycle assessment (LCA) to substantiate those sustainability claims.

Chapter 2

Batteries

2.1. Basics

A battery stores chemical energy and delivers electrical energy through a coupled redox reaction: one electrode is oxidized; the other is reduced. The term 'battery' may refer to a single electrochemical cell or to an assembly of multiple cells configured as a battery pack for practical application. Rechargeable batteries consist of a positive electrode (cathode during discharge) and a negative electrode (anode during discharge). The two electrodes are electronically connected through an external circuit, while ion transport between them is enabled by the electrolyte, illustrated in Figure 2.1.[16]

The potential difference between the electrodes determines the cell voltage, as shown in Equation 2.1, and can be calculated from the Gibbs free energy change (ΔG) of the reaction using the Nernst equation.

$$V_{cell} = -\frac{\Delta G}{nF} \qquad \textit{Equation 2.1}$$

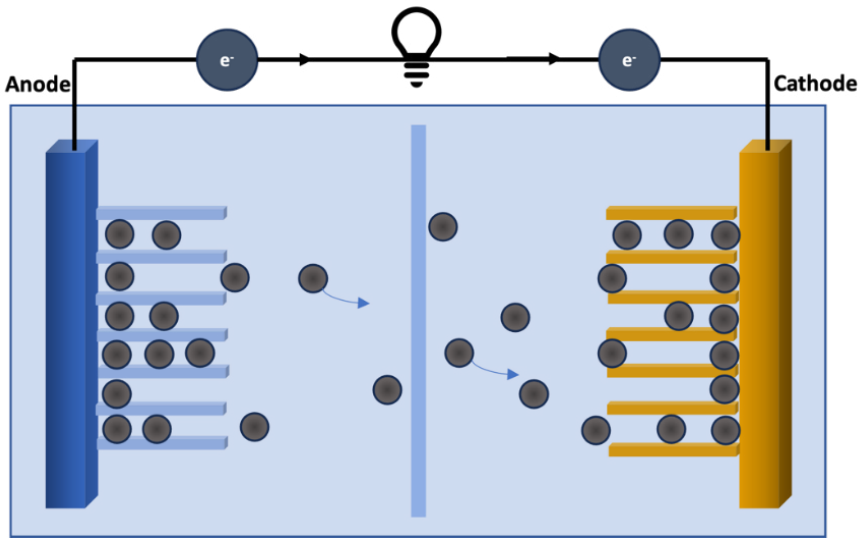

Figure 2.1. Illustration of an electrochemical cell during discharge.

Battery cell voltage, V_{cell}, is the electric potential difference between the cathode ($E_{cathode}$) and the anode (E_{anode}) within a battery system, as expressed by the equation:

$$V = E_{cathode} - E_{anode} \qquad \textit{Equation 2.2}$$

This cell voltage represents the driving force behind the movement of electrons during charge and discharge in a battery. The theoretical voltage sets an upper limit on this potential difference. The cell voltage varies with the state of charge (Q) and can be expressed as a function of V(Q), determined by the specific electrochemical reaction of the system. The total energy output of the cell is obtained from the integral in Equation 2.3, where C represents the reversible capacity, i.e., the maximum charge that can be efficiently transferred.

$$E = \int_0^C V(Q)dQ \qquad \textit{Equation 2.3}$$

2.2. Lithium Batteries

Lithium-ion Batteries

LIB emerged from Whittingham's 1970s demonstration of lithium intercalation, was enabled by Goodenough's layered oxide cathodes (e.g., $LiCoO_2$ and later NMC) that raised voltage and energy and became practical when Yoshino replaced lithium metal with a carbonaceous anode leading to Sony's 1991 commercialization. These breakthroughs were recognized by the 2019 Nobel Prize in Chemistry. Compared to conventional lead acid batteries, LIBs deliver much higher energy density and capacity.[1]

In modern cells, composite electrodes are cast onto metal current collectors: cathodes such as LFP or NMC are mixed with conductive carbon and a polymer binder (e.g., PVDF) and coated on aluminum foil, while anodes based on graphite or Si–graphite use conductive carbon and binders (e.g., PVDF or CMC/SBR) on copper foil. A porous polyolefin separator sits between them, wetted by a non-aqueous electrolyte, typically a lithium salt (e.g., $LiPF_6$) in carbonate solvents with tailored additives. Early cycling forms thin interphases, the solid–electrolyte interphases (SEIs) on the anode, that regulate ion transport and suppress unwanted reactions (Figure 2.2).

For a graphite|$LiCoO_2$ cell, the discharge can be written as:

Reduction at anode: $Li_xC_6 \rightarrow C6 + xLi^+ + xe^-$

Oxidation at cathode: $xLi^+ + xe^- + Li_{1-x}CoO_2 \rightarrow LiCoO_2$

Total reaction: $Li_xC_6 + Li_{1-x}CoO_2 \rightarrow C_6 + LiCoO_2$

During discharge, lithium is oxidized at the anode. The ions migrate through the electrolyte and intercalate into the cathode host where reduction occurs, and electrons simultaneously traverse the external circuit to power the load; the processes reverse on charge.

Because metallic lithium is highly reactive, commercial LIBs rely on these intercalation hosts for safety and longevity. [16] Even as research continues toward next-generation lithium-metal cells that promise higher specific energy but face other challenges.

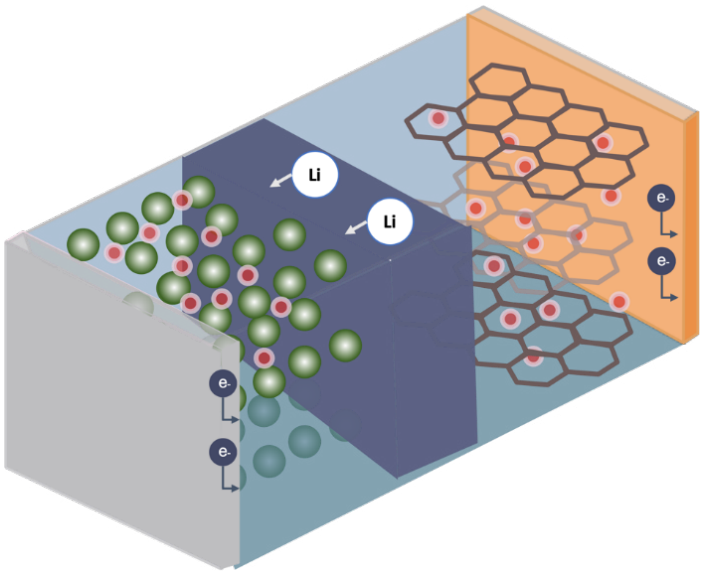

Figure 2.2. Illustration of a LIB setup showing positive and negative electrode materials, current collector, and separator.

Next-Generation Batteries: Lithium metal

Lithium metal batteries (LMBs) employ metallic lithium as the anode. The lithium metal anode has garnered significant interest due to its exceptional properties, including the highest theoretical specific capacity (3860 mA h g^{-1}) and the lowest anode potential (−3.04 V vs. the standard hydrogen electrode). [17–19] These characteristics make Li metal

an appealing candidate for advanced rechargeable batteries. However, practical implementation has been hindered by dendrite formation during charging, which poses safety risks and shortens cycle life. [20] Researchers are exploring diverse strategies to overcome these challenges and enable the development of next-generation LMBs.

2.3. Multivalent Batteries

LIBs have long dominated the field of portable electronics and electric vehicles due to their technological maturity, high energy density, and reliable performance. However, modern LIBs are approaching their theoretical limits, and their application in large-scale grid energy storage is hindered by several factors, including limited raw material availability, high costs, safety concerns, and finite cycle lifetimes. [5,8,21] These limitations have motivated the search for alternative battery chemistries beyond lithium.[22–24] Considerable attention has therefore turned toward earth-abundant and potentially more sustainable candidates such as sodium-ion (SIBs), potassium-ion (PIBs), magnesium (MgBs), calcium (CaBs), zinc-ion (ZIBs), and aluminum-ion batteries (AlBs). [22–24]

Multivalent batteries, characterized by the transfer of ions carrying multiple charges (e.g., Mg^{2+}, Ca^{2+}, Zn^{2+}, Al^{3+}), have emerged as a promising alternative to conventional lithium-ion batteries and represent a vital part of next-generation battery research.[24–33] Their fundamental advantage lies in the ability of multivalent cations to transfer more than one electron per ion. In principle, this enables higher capacities and energy densities compared to monovalent systems such as lithium or sodium. For instance, divalent ions such as calcium and magnesium carry two electrons per ion, theoretically doubling the charge-storage capacity relative to lithium if suitable electrolytes and electrodes can be developed.[34] In addition to this energy density advantage, multivalent systems also offer potential improvements in safety and environmental sustainability. [24–33]

CaBs are particularly promising due to calcium's natural abundance, low cost, and low toxicity. With a theoretical volumetric energy density significantly higher than conventional graphite-based lithium-ion batteries (2.06 Ah/cm^3 for calcium vs. 0.97 Ah/cm^3 for graphite), CaBs hold the potential to substantially surpass current lithium-ion performance metrics. [34–36] However, the development of viable calcium battery materials faces significant challenges, particularly related to the electrolyte stability, reversible calcium plating and stripping at the anode, and cathode material compatibility. [34]

The basic electrochemical reactions involved in calcium batteries are:

At the anode (metallic calcium anode):

$$Ca^{2+} + 2e^{-} \rightleftharpoons Ca$$

At the cathode:

$$Ca_y Host + xCa^{2} + 2xe^{-} \rightleftharpoons Ca_{x+y} Host$$

Despite this promise, several fundamental challenges remain. The major obstacle is achieving reversible plating and stripping of metallic calcium. Progress has been reported using specific electrolyte formulations, particularly salts such as calcium borohydride ($Ca(BH_4)_2$), calcium tetrafluoroborate ($Ca(BF_4)_2$), calcium perchlorate ($Ca(ClO_4)_2$), calcium bis-tetrakis(hexafluoroisopropyloxy)borate ($Ca(B(hfip)_4)_2$), and calcium bis(trifluoromethanesulfonyl)imide ($Ca(TFSI)_2$) dissolved in organic carbonate solvents.[35] Both computational and experimental studies have revealed that the solvation structure and free energy of solvation of Ca^{2+} are strongly dependent on the electrolyte environment, which in turn governs ionic conductivity and electrode compatibility. [35]

Furthermore, cathode development for CaBs is still in development, with limited materials demonstrating stable cycling and adequate capacities. Efforts are directed toward diverse material classes, including intercalation oxides, sulfides, organic electrodes, and sulfur-based systems.[36] However, achieving high-voltage operation with compatible electrolytes remains an outstanding challenge.

Overall, despite the evident potential and substantial theoretical benefits, considerable research efforts are necessary to overcome the technical challenges in electrolyte and electrode material compatibility. Future advancements will require coordinated computational, experimental, and methodological developments to realize multivalent batteries' practical applications and commercial viability.

Chapter 3

Electrolytes

Among the crucial components of a battery, the electrolyte plays a vital role in facilitating ion transport between the electrodes, thereby enabling efficient energy storage and release. For the electrolyte, key properties include high ionic conductivity (≥ a few mS cm^{-1}) while remaining electronically insulating; stability ≥ 4.5 V vs. Li^+/Li^0 (and ~0–5 V operation); operability from ~−20 to 180 °C; $\varepsilon_r \geq 20$; good wettability; and chemical compatibility with all components. Practically, low viscosity, high flash point/low flammability, low toxicity, low cost, and low environmental burden are also desired; trade-offs remain among different types of electrolytes. [50] Therefore, researchers have been exploring various electrolyte options to enhance battery performance. The challenge to find an electrolyte that can complement other battery components effectively has made researchers explore a wide range of chemical systems.

3.1. Highly Concentrated Electrolytes

Highly concentrated electrolytes (HCEs) are defined by a salt-to-solvent ratio that is far higher than conventional 1 M electrolytes, often in the 3–5 M range or higher.[37–39] At such concentrations, the solvent becomes insufficient to fully solvate the cations, forcing anions into the first solvation shell.[40] Figure 3.2 presents a schematic of local-structure changes with salt concentration. This “solvent-in-salt” regime reduces the number of free solvent molecules, resulting in structures dominated by contact ion pairs (CIPs) and cation-anion aggregates (AGGs).[12,41,42] In this sense, HCEs share similarities with ionic liquids, though with greater tunability via salt–solvent combinations.[42]

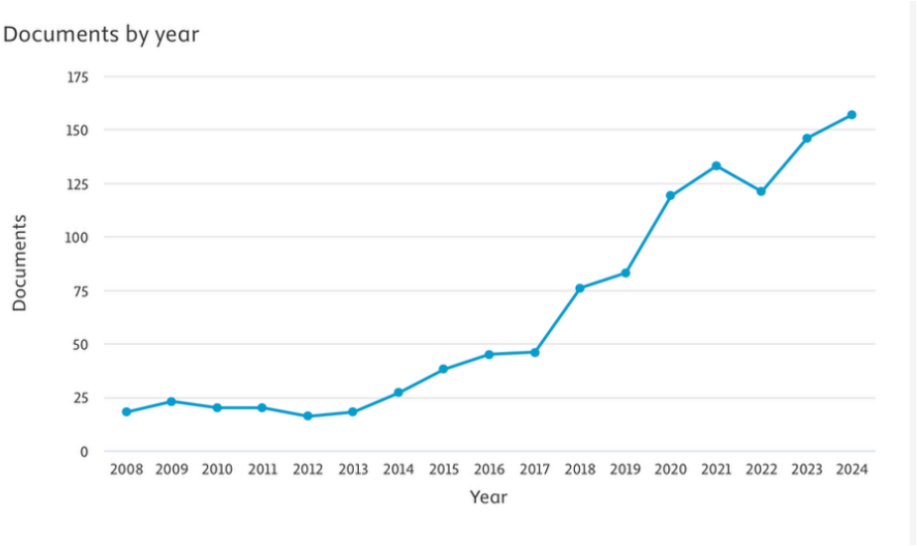

Figure 3.1. Trends in the number of publications using the keywords highly concentrated electrolytes on the Scopus database.

The altered solvation environment offers important electrochemical properties. Because free solvent is minimized, HCEs exhibit a broadened electrochemical stability window (ESW), suppress solvent decomposition, and enable cycling at both higher and lower electrode potentials than conventional electrolytes.[43,44] They also help mitigate aluminum current collector corrosion, suppress transition-metal dissolution from cathodes, and form anion-derived SEIs that stabilize anodes.[38,45] Furthermore, reduced vapor pressure and higher boiling points improve safety.[46]

The local structure of HCEs is dominated by extensive ion aggregation, which profoundly alters their dynamics compared to dilute solutions. In the concentrated regime, solvent molecules are fully engaged in cation solvation, leading to coordination environments enriched with anions and resulting in extended networks of CIPs and AGGs.[40–42,47–50] This aggregation decreases the population of free solvent and creates heterogeneous local domains with distinct transport properties.[38,46] Yamada and co-workers[46] have shown that such structural heterogeneity underlies the widened ESW, as reactive solvents are effectively shielded within aggregates. Jiang et al.[38] further emphasized that this network-like ion organization leads to spatially correlated motion, where clusters of ions move cooperatively rather than as isolated solvated species.

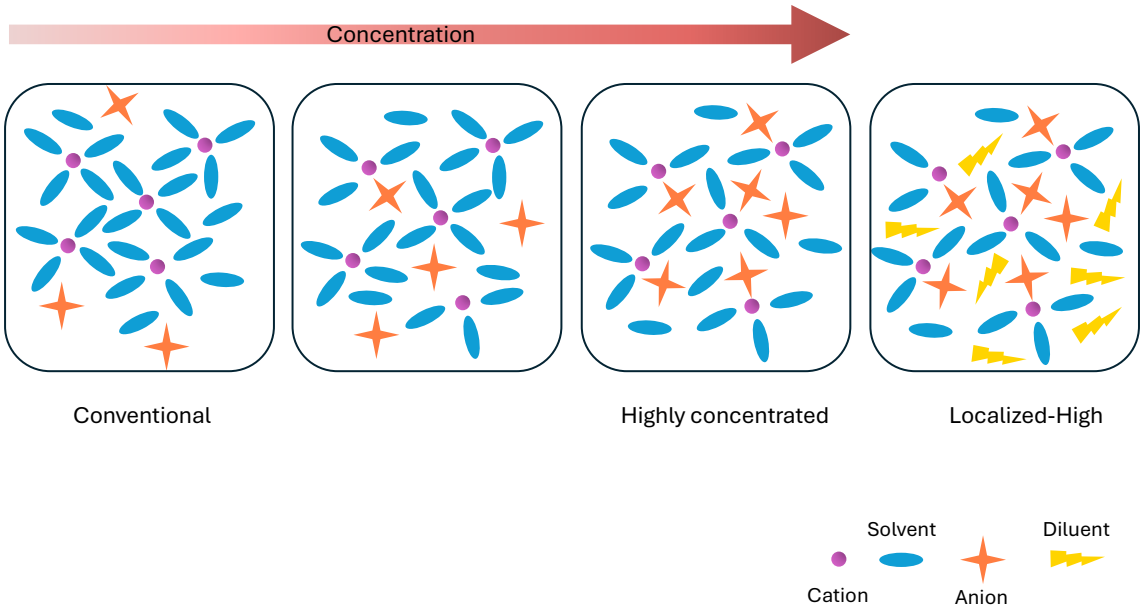

Figure 3.2. Schematic of the local structure across salt concentrations..

Yet the advantages of highly concentrated electrolytes come with practical costs, such as high viscosity, reduced conductivity, poor wetting, and higher expense. Localized high-concentration electrolytes (LHCEs) address this by introducing a weakly solvating diluent that preserves the primary solvation environment while lowering viscosity and improving wettability, thereby keeping HCE-like interfacial behavior with better processability and transport.[19,51–53]

Computational studies have become essential for understanding these unconventional phenomena. AIMD simulations have elucidated the coordination structures of cations in anion-rich environments, highlighting how partial solvation and aggregate formation dictate ESW and SEI composites. Polarizable force fields are increasingly applied to capture dielectric saturation, ion correlations, and the dynamic heterogeneity characteristic of HCEs, offering insights beyond fixed-charge models. Ab initio MD and polarizable force field simulations reveal dynamic heterogeneity in which fast ion channels coexist with immobilized aggregates, providing a microscopic origin of the partial decoupling between viscosity and conductivity often observed in HCEs.[53] Taken together, these results indicate that the unusual transport behavior of HCEs is not simply a consequence of high density but emerges from the interplay of anion-rich solvation,

aggregate formation, and correlated dynamics, and such approaches are critical for bridging experimental observation and molecular-level mechanisms

In this thesis, **Paper V** addresses sodium-based HCEs. The systems investigated consisted of NaTFSI in adiponitrile (ADN) at different salt-to-solvent ratios (1:2, 1:3, 1:4, 1:5, 1:6, 1:7, and 1:11). The computational contribution focused on analyzing the solvation structure and ion coordination environments across this concentration series. The chemical structures of NaTFSI and adiponitrile are shown in Figure 3.3.

In the context of calcium and sodium batteries, HCEs are especially promising. Ca electrolytes in dilute regimes suffer from sluggish plating/stripping and unstable SEIs, while Na metal systems face similar challenges with dendritic growth and parasitic side reactions. Concentrated formulations enforce anion-rich solvation, generating inorganic-rich SEIs and widening the ESW to enable more reversible metal cycling.

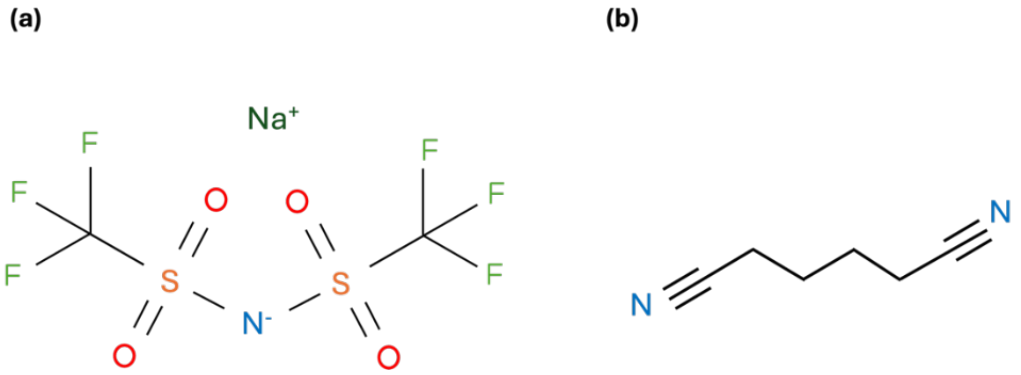

Figure 3.3. Structures of a) NaTFSI, b) ADN

For sodium, LHCEs have already demonstrated stable plating/stripping with high Coulombic efficiency and dendrite suppression.[54] Similar strategies are now being applied to calcium, where initial studies indicate that HCEs can mitigate long-standing interfacial challenges and may enable room-temperature Ca cycling.[55] Extending these principles to Ca-based deep eutectic electrolytes offers a promising route toward advancing both multivalent and alkali metal battery chemistries.

3.2. Deep Eutectic Electrolytes

3.2.1. Basics

DEEs, derived from deep eutectic solvents (DESs), are promising battery electrolytes because their properties can be finely tuned through the choice and ratio of constituents. However, the exploration of DEEs is still in its early stages. The surge in DEEs publications in recent years is shown in Figure 3.4. A deep eutectic solvent refers to a eutectic mixture comprising pure compounds that create a solution with a lower melting temperature compared to an ideal liquid mixture. Abbott et al. [56] have first coined the term DES in 2003 using a mixture of choline chloride (ChCl) and urea (U). However, the use of deep eutectic solvents was around before that as a way to lower the melting point of molten salts.

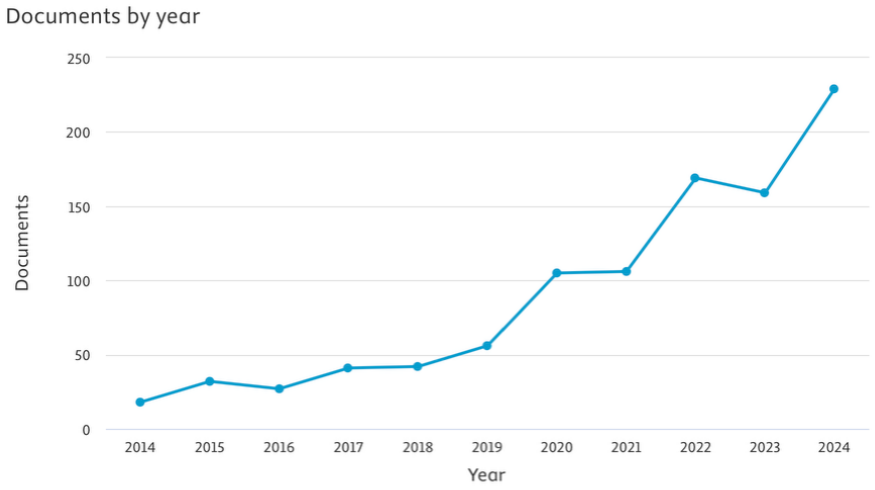

Figure 3.4 Trends in the number of publications using the keywords Deep Eutectic and electrolyte on the Scopus database.

Literature has shown that the use of DEEs has many advantages, such as providing high energy density and great thermal stability due to their low vapor pressure and high electrochemical stability window. However, their ionic conductivity remains relatively lower compared to other organic electrolytes.

Initially, the classification of deep eutectic solvents (DESs) relied on the presence of hydrogen bonding among their constituents, involving a hydrogen bond donor (HBD) and a hydrogen bond acceptor (HBA). This strong hydrogen bonding creates a charge

delocalization that presumably is the cause of a lower melting point than any of the forming components [57], although it is yet debated of which is the root cause. However, a more recent and refined definition places greater emphasis on the temperature depression observed in a phase diagram as a crucial characteristic of a deep eutectic solvent. This temperature depression is denoted as the difference (ΔT) between the simple eutectic point (TE, simple) and the deep eutectic point (TE, deep), as illustrated in Figure 3.5. Electrolytes with lower melting points, such as DES systems that show similar characteristics to ionic liquids (IL), offer a possible advantage to LIBs or lithium metal batteries by providing enhanced safety compared to traditional electrolytes, which may pose ignition risks[58,59].

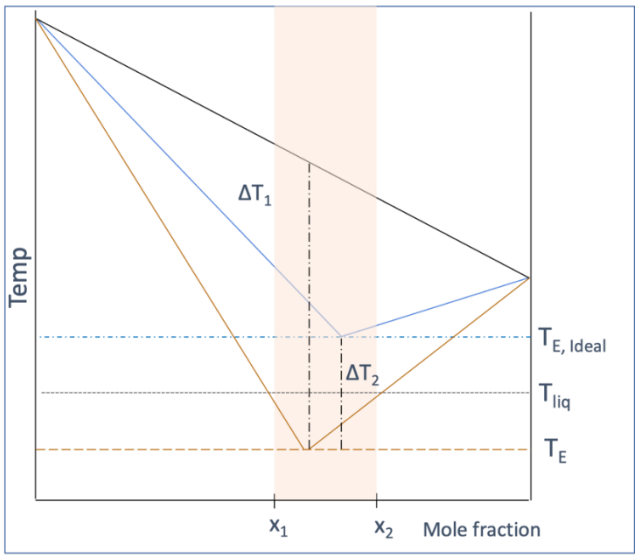

Figure 3.5. A comparison of the SLE of a simple ideal eutectic mixture in blue and a deep eutectic mixture in brown is shown schematically.

While DESs similarity to ionic liquid IL and class has been debated, Abbott et al. explain that they hold some key differences. While both share many properties, DES consists of a eutectic mixture formed by combining Lewis or Brønsted acids with bases, encompassing a diverse range of anionic and/or cationic species. In contrast, ionic liquids (ILs) are constituted primarily by one type of discrete anion and cation in their systems[60].

3.2.2. Types

Abbott et al. [61] described DESs with the general formula shown in Equation 3.1. They describe that the cationic component (Cat+) can encompass a wide range of species,

including ammonium, phosphonium, or sulfonium cations. On the other hand, the anionic component (X) typically involves Lewis bases, often represented by halide anions. These DESs can form complex anionic species by interacting with Lewis or Brønsted acid Y, where 'z' denotes the number of Y molecules interacting with the anion.

$$Cat^+ X^- \text{zY} \qquad \textit{Equation 3.1}$$

The classification of DESs is largely based on the type of complexing agent employed, as illustrated in Table 1. This classification takes into account the diverse combinations of cations and anions, resulting in a broad spectrum of properties and applications for deep eutectic solvents. In **Papers I, II, and IV**, the systems investigated fall under Type IV DESs, where a metal salt interacts with an HBD to form the eutectic mixture. This class is particularly relevant for electrolyte design, as the metal salt not only participates in the structural network of the DEEs but also serves directly as the charge carrier.

Table 1. Deep eutectic solvents classification adapted from Abbott et al.[61]

TYPE	GENERAL FORMULA	TERM	EXAMPLE
I	Cat+X-zMCl$_x$	Metal salt + organic salt	$ZnCl_2$ + ChCl
II	Cat+X-zMClx·yH2O	Metal salt hydrate + organic salt	$CoCl_2 \cdot 6$ H2O + ChCl
III	Cat+X-zRZ	Organic salt + HBD	ChCl + U
IV	MCl$_x$ + RZ = MClx-1+·RZ + MCl$_{x+1}$	Metal salt (hydrate) + HBD	$ZnCl_2$ + U

3.2.3. Battery Application

DEEs represent a novel class of electrolytes, are part of the broader category of deep eutectic solvents, and in this thesis, will be used interchangeably depending on the specificity needed. In recent years, DEEs have garnered increasing attention within the

research community due to their unique proclaimed properties, including cost-effectiveness, easy preparation, and environmental friendliness, depending on the composition. Particularly, DESs derived from metal salts -among others- to be used as electrolytes, often referred to as DEEs, hold promise as potential electrolyte candidates due to their homogeneity with a single cationic species and favorable ionic conductivity[59]. These unique attributes have sparked significant interest in exploring the applications and advantages of DEEs in various electrochemical systems.

DEEs have been used in lithium metal batteries as an alternative to traditional carbonate-based electrolytes that pose limitations on such battery systems. Using carbonate electrolyte against lithium metal anode raises concerns regarding dendritic lithium penetration and accumulation of inert dead lithium, which in turn results in poor interfacial stability and high reactivity of lithium metal against carbonate electrolytes.[18] Several cases of DEEs being employed in the context of lithium metal batteries have been documented in the literature. For instance, LiTFSI in combination with DpyDS has been used in one study[59]. Additionally, a different work by Hu et al [18] introduced a dual-anion deep eutectic solution (D-DES) by employing succinonitrile (SN) in conjunction with lithium salts (LiDFOB and LiTFSI).

DEEs have also found application in Li-ion battery systems, as evidenced by the work of Boisset et al.[58], who investigated N-methylacetamide (NMA) paired with various lithium salts (LiX, where X represents bis[(trifluoromethyl) sulfonyl] imide, TFSI; hexafluorophosphate, PF6; or nitrate, NO3), demonstrating the successful incorporation of LiTFSI-based DEEs into LIBs with advantageous attributes.

In **Paper I**, we present lithium-based DEEs composed of the hydrogen bond donor N-methylacetamide (NMA) with three salts of contrasting geometry: $LiBF_4$, LiDFOB, and LiBOB. The study focused on how these differences in anion symmetry and size influence solvation and hydrogen-bonding networks. The molecular structures of the investigated salts are shown in Figure 3.7.

A related group of lithium-based DEEs is formed with LiFSA and urea derivatives. **Paper IV** investigated systems prepared from LiFSA with urea and 1,3-dimethylurea (DMU) at different stoichiometries (e.g., LiFSA: Urea 1:4, LiFSA :DMU 1:2, LiFSA:Urea: DMU 1:1:1), with simulations analyzing ion coordination and solvent interactions. The chemical structures of LiFSA and the urea-based components are presented in Figure 3.6.

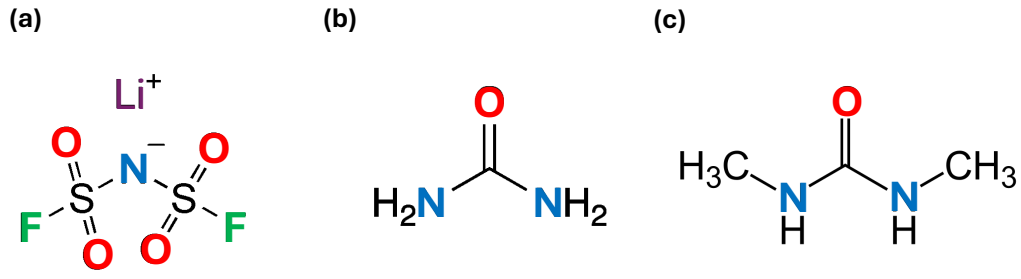

Figure 3.6. Structures of a) LiFSA b) Urea c) 1,3-DMU

Moreover, DEEs have extended their scope beyond lithium-ion and lithium-metal batteries, encompassing post-lithium-ion batteries involving sodium-ion, magnesium, aluminum-ion, and calcium batteries.[62]
In this context, **Paper II** investigated calcium-based DEEs combining NMA with BF_4, DFOB, BOB, and the larger symmetric Bhfip anion. The analysis concentrated on the effect of multivalent cations on solvation and coordination structure. The chemical structures of these salts are shown in Figure 3.7. Finally, **Paper III** mentions future outlooks for liquid electrolytes, including deep eutectic solvents to be used in multivalent batteries.

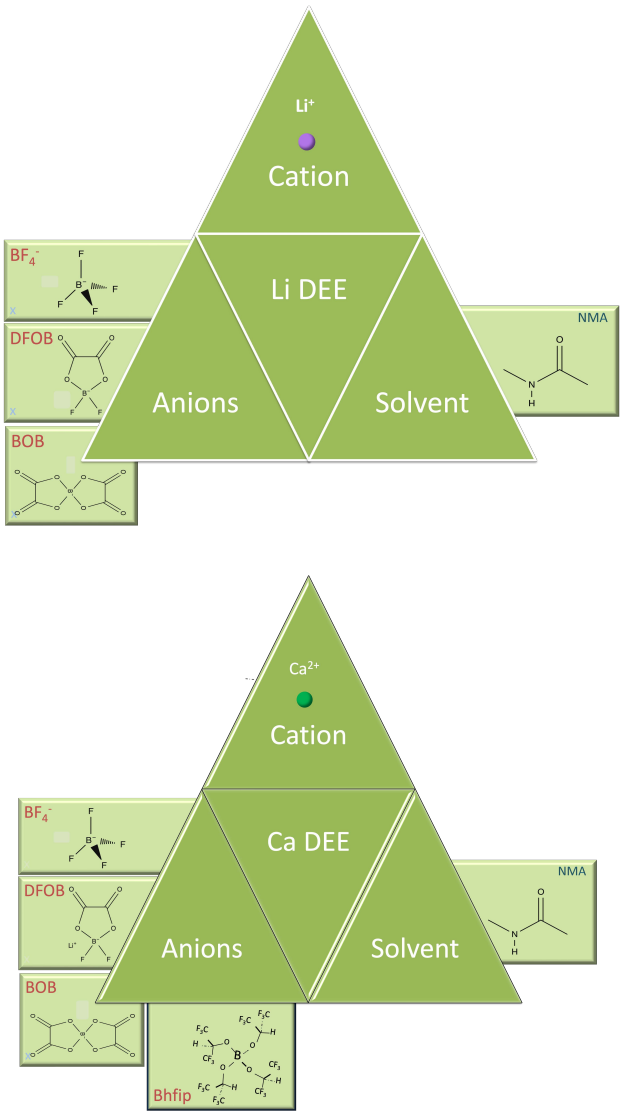

Figure 3.7 structures of studied DEEs components: a) lithium DEE, b) calcium DEE

3.2.4. Molecular-Level Heterogeneity (MLH)

DESs exhibit ordering supported by extensive hydrogen bonding among all components; in reline, the choline hydroxyl participates in a connected HB network, and the liquid shows a layered local structure rather than a random arrangement.[65] Many DESs also show nanometer-scale organization, reflected in features assigned to intermediate-range structure; in hydrophobic systems, this organization is linked to clustering of polar groups sustained by hydrogen bonds.[66,67] In many studies, Microheterogeneity (MH) is described as partial separation of polar and non-polar parts, strengthened by longer side chains and accompanied by subtle changes in the HB network within polar regions.[68] Ultrafast vibrational spectroscopy on amide-based DESs separates a fast (~1 ps) HB making and breaking component from a slower contribution that correlates with HBA asymmetry and polarity, the behavior is rationalized by microscopic heterogeneities that slow HB exchange in specific environments.[69] Another paper describes how composition can also steer heterogeneity. In KSCN/acetamide mixtures, increasing water content drives more parallel alignment of SCN^- and growth of larger water clusters, indicating composition-controlled non-uniformity.[70] Dynamically, DESs can display fractional Stokes–Einstein behavior and, in at least one salt mixture, a non-canonical relation between the extent of SE breakdown and dynamic heterogeneity, so transport decoupling is not a one-number proxy for heterogeneity.[71]

In **Paper I**, molecular-level heterogeneity (MLH) is defined as the heterogeneous organization of the hydrogen-bond network originating from differences in the size, charge, and shape of the components. This heterogeneity is expressed in coordination and solvation differences and as dispersion in dynamical properties such as self-diffusion, thereby producing non-uniform behavior that impacts the performance of DEEs.

In order to understand and measure heterogeneity in DESs, prior work have used several techniques, depending on the definition, specifically to isolate it from general structure. MD-guided scattering identifies pre-peaks in S(q) as signatures of nanometer-scale organization and domain formation, which can be enhanced by longer alkyl chains.[67,68] Domain analysis within MD resolves polar/non-polar segregation and shows its indirect effect on the HB network in polar regions.[68] Ultrafast 2D-IR isolates HB exchange components that vary with HBA polarity/asymmetry, supporting a microscopically heterogeneous landscape.[69] Quasielastic and elastic incoherent neutron scattering probe

mobility distributions and reveal fractional SE behavior, with one study showing an anticorrelation between SE breakdown and dynamic heterogeneity across salts.[72]

Pair correlations and HB distributions describe local order, but they do not fully capture the heterogeneity that arises from the interplay of multiple structural and dynamical factors. To address this, we developed in **Paper I** an MLH index to integrate diverse descriptors into a single comparative measure.

The MLH index is defined as:

$$MHI = \sum_i w_i f_i \qquad \textit{Equation 3.2}$$

where f_i are normalized molecular features and w_i their weights, constrained so that $\sum_i w_i = 1$. The chosen descriptors included:

1. Hydrogen-bond localization factor (derived from a Gini coefficient to quantify unevenness in HB distribution).
2. Relative diffusion coefficients of anions and solvent (D_anion / D_NMA).
3. Anion size, representing steric influence on solvation.
4. Anion solvation number, obtained from coordination analysis.
5. Symmetry descriptors of the anion.

All features were normalized to their maximum values to avoid unit dependence. For descriptors inversely correlated with heterogeneity (e.g., diffusion ratio, symmetry), the transformation $1 - \widehat{f_i}$ was applied to align interpretation with the directionality of MLH. With these definitions, equation 3.2 can be explicitly written as,

$$MHI = w_1 \hat{L}_{HB} + w_2 \left(1 - \widehat{D}_{\frac{anion}{NMA}}\right) + w_3 \hat{S}_{anion} + w_4 \widehat{SN}_{anion} + w_5 (1 - \hat{\Sigma}_{symm})$$

Equation 3.3

Weights were determined through a two-step hybrid approach. First, principal component analysis (PCA) identified which descriptors contributed most to the variance across electrolytes. Because PCA emphasizes statistical variance rather than physicochemical

meaning, weights were then refined using correlation analysis to ensure alignment with features most relevant to heterogeneity. This hybrid approach balances statistical rigor with physical interpretability.

Alternative weighting schemes (such as uniform weights or PCA-only) were also tested, and while overall MLH trends were preserved, the hybrid method provided greater resolution and better correspondence with qualitative observations.

Looking forward, several computational analyses not used here could deepen the MLH picture in DESs. Cluster/domain analysis on atomic coordinates or HB graphs would yield size distributions of aggregated regions and connect directly to the domain-level views reported in MD work. Percolation and lifetime analysis on HB/coordination networks would locate connectivity thresholds and residence-time spectra associated with persistent regions, complementing the network-centric interpretation of DEEs structure.

Chapter 4

Computational Approaches

4.1. Molecular Dynamics

Molecular dynamics (MD) numerically integrates the equations of motion for interacting particles to connect microscopic structure and dynamics with macroscopic observables. Depending on how forces are obtained, MD is carried out either with empirical force fields (classical MD) or by computing forces from electronic structure on-the-fly (ab initio MD). In practice, simulations proceed by preparing an initial configuration, equilibrating the system, and then sampling trajectories to obtain equilibrium and transport properties from time-averaged observables.[73]

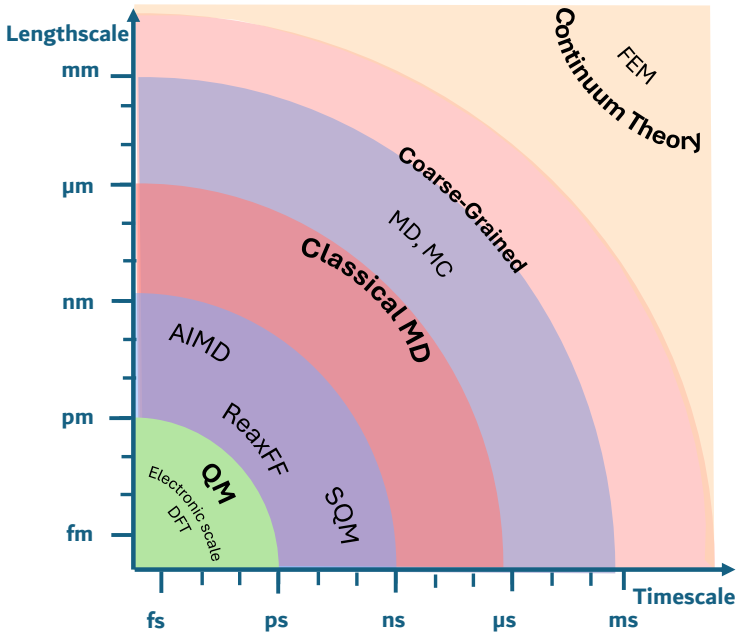

Figure 4.1. Illustration of time and length scales of different simulation frameworks.

4.1.1. Classical MD

Molecular dynamics simulation is a powerful tool used to simulate the structure and behavior of atoms and molecules, providing insight into materials' thermodynamics, structure, and geometry in a classical framework. The atoms are represented as single point masses within van der Waals potentials, and their positions and velocities are used to solve Newton's equations of motion based on force fields (FF) without treating electrons explicitly.

The Born-Oppenheimer approximation justifies the separation between electronic and nuclear motions, as the time scales of these motions differ significantly due to the large mass ratio between nuclei and electrons[74]. In classical force fields, electronic interactions are implicitly considered in an averaged and effective manner. By adopting a classical approach to model atoms, computational efficiency is enhanced, which enables simulations of larger systems over longer time spans. This approximation allows researchers to efficiently study the dynamic behavior of complex systems without explicitly calculating electronic motions, thereby saving computational resources and facilitating the exploration of a wide range of phenomena[74].

The equation of motion derived from Newton's laws for a system comprising N particles interacting through a potential $U(\vec{r}i)$, $i = 1,\ldots,N$, can be expressed as the two first-order differential equation 4.1:

$$\begin{cases} \dot{\vec{r}}_i = \frac{\dot{\vec{p}}_i}{m_i} \\ \dot{\vec{p}}_i = \vec{F}_i \end{cases}, \qquad \textit{Equation 4.1}$$

Where $\dot{\vec{r}}_i$ describes the derivation of $\vec{r}_i$ in terms of time and m_i is the mass of particles. While the force $\vec{F}_i$ is expressed as,

$$\vec{F}_i = \frac{\partial U(\vec{r}_i)}{\partial(\vec{r}_i)} \qquad \textit{Equation 4.2}$$

The equation of motion can be represented by Equation 4.1 or a second-order equation and thus to simulate the motion of N particles in three dimensions at each time step, it is needed to solve either a set of 3N second-order differential equations or an equivalent set of 6N first-order differential equations[74].

4.1.2. AIMD

In first-principles ab initio molecular dynamics (AIMD), interatomic forces are not described by fixed empirical potentials but are computed on-the-fly from quantum mechanical electronic structure calculations, most commonly based on density functional theory (DFT).[75]

Within the Born–Oppenheimer approximation, the electronic subsystem is assumed to remain in its instantaneous ground state while the nuclei move. For each nuclear configuration, the electronic Schrdinger (Kohn–Sham) equations are solved to obtain the ground-state energy, and the nuclear forces are then derived as its gradients, Hellmann–Feynman forces, with Pulay corrections when the basis set depends on atomic positions. These forces enter Newton's equations of motion, which are integrated to propagate the nuclei.

$$M_I \ddot{R}_I = F_i = -\nabla_{R_i} E$$

Equation 4.1

,

where M_I and $\ddot{R}_I$ are mass and acceleration of atom I, respectively, Fi is the force acting on it. This approach differs fundamentally from classical MD, where interatomic interactions are defined by fixed analytical potentials. In AIMD, the electronic Hamiltonian itself generates the interactions, removing the need for fitted force-field parameters. Several formulations exist, the most common being Born–Oppenheimer molecular dynamics (BOMD), where the electronic structure is fully converged at each step, and Car–Parrinello molecular dynamics (CPMD), which introduces fictitious electronic masses so that the orbitals evolve alongside the nuclei.[76]

The computational expense of solving the electronic problem at every time step restricts AIMD to modest system sizes, typically hundreds of atoms, and short timescales in tens of picoseconds. By contrast, classical MD can simulate tens of thousands of atoms over nanoseconds. Despite these limitations, AIMD provides predictive accuracy in cases where empirical force fields are unreliable, such as bond breaking and formation, charge transfer, or strongly ionic and hydrogen-bonded environments.[75]

4.2. Semi-empirical Quantum Mechanical (SQM) methods

Using quantum mechanical methods to predict materials structure or behaviour by calculating their electronic structure has been a great way to understand chemical compounds better and save more experimental time. DFT has been an indispensable and common tool used in such calculation due to it finding the specific solution of a Schrödinger equation, using ab initio quantum mechanical methods, however this yields to be very costly. Therefore, SQM are used alternatively for larger systems since they are computationally more efficient and faster by two folds but comes at a cost of decreased accuracy compared to DFT[77]. They describe the electronic structure of molecules using mathematical equations and parameters that are derived from empirical data or higher-level quantum mechanical calculations. They utilize a more simplified description of electron-electron interactions while neglecting explicit treatment of all electron-electron repulsion integrals, which are more computationally demanding [78].

There are various SQM methods that are based on molecular orbital (MO) theory. The initial parameterization of these MO methods was formulated with the aim of accurately reproducing ab initio Hartree-Fock (HF) results achieved using a minimal basis set.[78] Some notable examples are the complete neglect of differential overlap (CNDO) method[79], the intermediate neglect of differential overlap (INDO) method[80] and neglect of diatomic differential overlap (NDDO). Two NDDO-based methods resulted in MNDO[81] and AM1[82]. Later, PM3[83] method was a result of parameterization of MNDO. **Paper V** utilizes an SQM software molecular orbital package (MOPAC)[84] in which the MO are obtained through The semiempirical Hamiltonians MNDO, AM1, PM3 , PM6, RM1, MNDO-d[85,86], and PM7 are used in the electronic part of the calculation. These methods have demonstrated success in reasonably predicting various molecular properties, including geometries, electronic energies, and spectroscopic characteristics.[87]

The interest in semiempirical quantum mechanical (SQM) methods has been renewed with the introduction of the density functional tight binding (DFTB) method, which was pioneered by Seifert, Elstner, and Frauenheim[88–90]. This advancement has sparked renewed attention and research in the field.

4.2.1. Tight-Binding Methods

A commonly use SQM method is the tight-binding (TB) method. TB is a linear combination of atomic orbitals (LCAO) method and used to investigate the band structure and single-particle Bloch states of materials. Its notable advantage is its computational efficiency, making it suitable for analyzing electronic properties in large systems containing thousands of atoms within the unit cell. Through the incorporation of empirical parameters, the tight-binding method simplifies calculations while still providing reliable insights into the electronic structure of complex materials.

4.2.2. DFTB

DFTB is a powerful approximation method that combines aspects of DFT and TB methods. It employs atom-centered orbitals and density fitting techniques to efficiently calculate molecular properties. The DFTB approach combines the computational efficiency of ZDO based approximations, which date back to the 1970s[78], with the improved accuracy compared to traditional HF methods provided by DFT[15]. While DFT gained popularity due to its higher accuracy, SQM methods like DFTB have advantages in studying specific systems and chemical properties. However, it is important to note that SQM approaches, including DFTB, may not offer the same level of accuracy for different chemical properties as DFT. To address this limitation, the development of the xTB method aimed to bridge the gap and provide more accurate results for a wider range of chemical properties.

4.2.3. xTB

The x in the name xTB stands for ‘extended’ to highlight the availability of parameters covered for nearly the complete periodic table of elements, it also denotes extensions in the AO basis set and the Hamiltonian's setup. xTB incorporates approximations for the Hamiltonian and electrostatic energy that are akin to those used in DFTB3 and zero-differential overlap (ZDO) methods during its parameterization[15]. In the case of GFN1-xTB[87], the approach utilizes similar approximations for the Hamiltonian and electrostatic energy, mainly second-order with some terms extended to third-order, as observed in DFTB3. However, unlike DFTB3, GFN1-xTB does not depend on an atom pair-wise parameterization.

The balance between accuracy and speed is achieved by employing a hierarchy of multiple levels of complexity. The working principle of this multilevel modelling is that

the method initially scans for a wide range of candidate molecules, solving a larger number of calculations using a GFNn-xTB method. In the next level, the number of candidates is lowered while the theory accuracy of a density functional theory DFT calculation is increased. Finally, a smaller group of candidates is determined, where those structures are handled with a high-level theory of DFT or wave function theory (WFT) to resolve the thermodynamic state with higher accuracy.

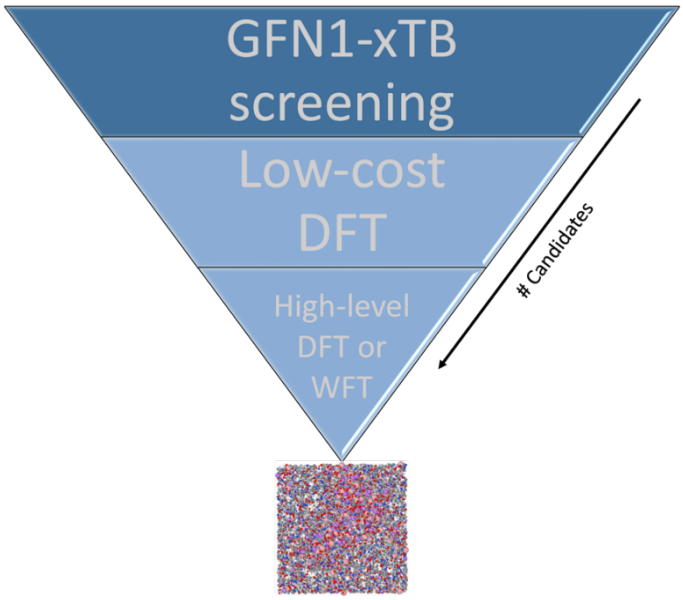

Figure 4.2. A schematic representation of the hierarchy of different theory levels used in xTB based on the GFN method, adapted from Bannwarth et. al [91]

GFN1-xTB offers a variety of advantageous characteristics compared to other QM and FF methods according to Grimme's group [77,87]. First, it provides structural information for systems around equilibrium to calculate properties such as noncovalent interactions and vibrational frequencies. Using an ab initio method to obtain such properties is challenging for larger systems, and it is less accurate than SQM methods for properties such as chemical reaction energies, since they are not included in the training set [87].

The use of small AO basis sets in most semi-empirical approaches constrains their accuracy and their ability to produce physical results. While the GFN1-xTB method enhances hydrogen bonding representation and d-polarization functions by using a second hydrogen s-function in the minimal basis set of atom-centered, approximate Slater functions [87].

Another appealing facilitation of the GFN1-xTB method is that it is pre-parameterized using reference data from hybrid DFT calculations; therefore, there is no need for a pair-

specific potential in the input file. This greatly saves effort by simplifying the input needed since it provides both global and element-specific parameters. Lastly, compared to other semi-empirical methods, it is more versatile as it provides information on properties for a wider range of chemical systems covering most of the periodic table with higher accuracy [77].

The total energy expression for GFN-xTB is represented by the electronic (E_{el}), atom pairwise repulsion (E_{rep}), dispersion (E_{disp}), and halogen-bonding (E_{XB}) terms:

$$E = E_{el} + E_{rep} + E_{disp} + E_{XB} \qquad \textit{Equation 4.3}$$

The electronic energy represented by E_{el} term is calculated using the Equation 4.4,

$$\begin{aligned} E_{el} &= \sum_{i}^{occ.} n_i \langle \psi_i | \mathrm{H}_0 | \psi_i \rangle \\ &+ \frac{1}{2} \sum_{A,B} \sum_{l(A)} \sum_{l'(B)} p_l^A p_{l'}^B \gamma_{AB,ll} \\ &+ \frac{1}{3} \sum_{A} \Gamma_A q_A^3 - T_{el} S_{el} \end{aligned} \qquad \textit{Equation 4.4}$$

Where n_i is the occupation number and ψ_i is the valence MOs and H_0 is the zeroth order Hamiltonian.

We implemented the xTB method in most papers in this thesis. In **Paper I**, we examined Li-based DEEs of NMA with $LiBF_4$, LiDFOB, and LiBOB to probe how anion geometry and symmetry, as well as hydrogen bonding, shape local structure and heterogeneity. In **Paper II**, we extended to Ca based DEEs with $CaBF_4$, CaDFOB, CaBOB, and Bhfip, to assess the impact of multivalent and bulkier/symmetric anions on coordination and structural organization. In **Paper IV**, we studied LiFSA eutectics with urea and DMU across multiple stoichiometries to evaluate how hydrogen bond donor identity and composition govern the solvation environment and HB topology.

4.3 Local Structure and Dynamics

Understanding electrolytes at the molecular level requires a set of complementary analyses, chosen according to the question at hand. One way to understand local structure

is to employ radial distribution functions (RDFs) to quantify radial correlations and to derive coordination numbers, partial coordination numbers, and cumulative distributions around a chosen reference species. For problems focused primarily on nearest-neighbor structure and solvation counts, RDFs alone are sufficient and are therefore used as a structural descriptor. When orientational detail interactions are important, RDFs are supplemented with spatial distribution functions (SDFs), which map three-dimensional preferences, and with hydrogen-bond analyses, using standard distance/angle criteria, distance distributions, and distance/angle maps. To probe dynamical properties, the time evolution of atomic positions is analyzed through the mean-squared displacement (MSD), from which self-diffusion coefficients are extracted. The following subsections present the theoretical background and implementation of these tools in this thesis.

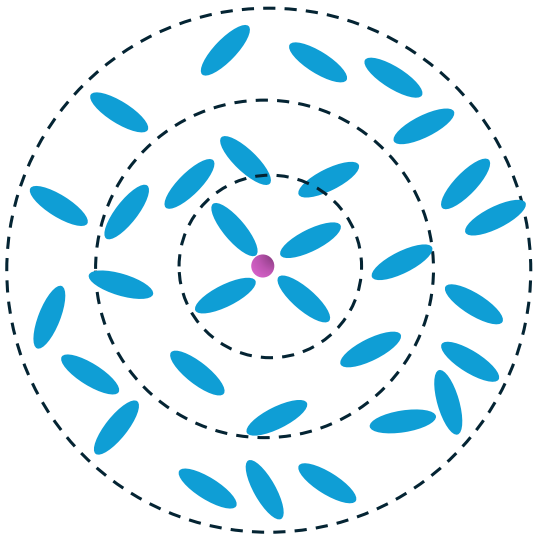

Figure 4.3. Illustration of a solvation shell where solvent molecules coordinate a cation.

4.3.1 Radial Distribution Functions and Coordination Numbers

The first step in analyzing the simulations was to compute radial distribution functions (RDFs), g(r), which quantify how the probability of finding two atoms varies as a function of their separation. RDFs were calculated for all relevant atom pairs using VMD.[63] Mathematically, the RDF is defined as:

$$g(r) = \lim_{dr \to 0} \frac{p(r)}{4\pi \left(\frac{N_{pairs}}{V}\right) r^2 \, dr} \qquad \textit{Equation 4.5}$$

where V is the total volume, $p(r)$ is the average number of atom pairs found between r and $r + dr$, and N_{pairs} is the number of unique pairs considered.

Coordination numbers (CNs) were obtained by integrating g(r) up to the first minimum beyond the main peak (Fig. 4.4), representing the number of neighbors in the first solvation shell. Partial RDFs were also computed for specific atom types (e.g., Ca–O, Ca–F, or anion–NMA), yielding partial coordination numbers (pCNs). By accumulating these values as a function of distance, cumulative distribution functions (CDFs) were constructed. CDFs are particularly useful as they provide insight into how coordination builds up incrementally with distance. Solvation numbers (SNs) were obtained by summing contributions from cation–anion and cation–solvent interactions.

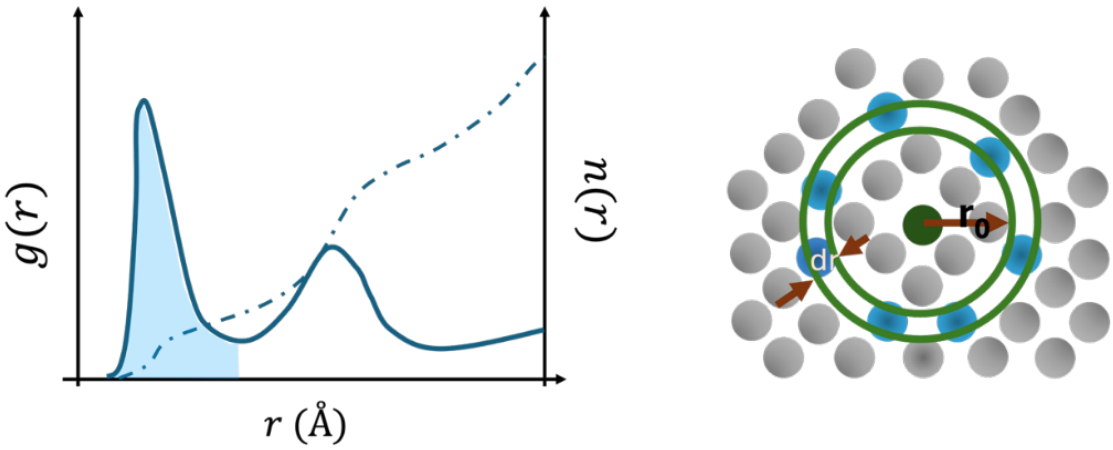

Figure 4.4. Illustration of an RDF plot with CN integration pointed and spherical-shell binning.

Spatial Distribution Functions (SDFs)

Although RDFs give information about radial correlations, they are spherically averaged and therefore cannot resolve orientation or angular dependencies. To provide a three-dimensional description, spatial distribution functions (SDFs) were calculated with TRAVIS.[64] SDFs are generated by superimposing many trajectory frames to record the spatial probability density of selected species relative to a reference, such as the cation. The resulting isospherical maps highlight where solvent molecules and anions are most likely to be located, revealing preferential orientations that RDFs don't always fully capture.

For example, SDFs centered on Ca^{2+} can show whether solvent carbonyl groups coordinate symmetrically or whether anions occupy particular orientations in the first solvation shell. In this way, SDFs provide complementary information to RDFs, allowing both radial and spatial aspects of solvation structure to be understood.

4.3.2 Hydrogen Bonding (HB) Analysis

Hydrogen bonds were detected directly from the MD trajectories with an in-house Python workflow. The script (i) loads per-frame atomic coordinates, (ii) assembles donor/acceptor sets (NMA N–H as donors; anion electronegative sites oxygen or fluorine as acceptors, with explicit exclusion rules where needed to avoid misassignment), and (iii) A contact was classified as an HB when the hydrogen–acceptor distance (H···A) ≤ 3.5 Å and the donor–H···acceptor angle ≥ 150°; for each event we stored the H···A distance, the D–H···A angle, the D···A distance, and (optionally) the donor–acceptor midpoint.

HB PDF

Distances of qualified HB pairs were binned to obtain a probability density in distance,

$$\hat{p}(r_k) = \frac{n_k}{N_{HB}\Delta r} \qquad \textit{Equation 4.6}$$

where n_k is the number of HB events in bin k of width Δr, and N_{HB} is the total number of HB detections. The resulting bar plot (probability density on the y-axis vs. radial distance on the x-axis) summarizes how frequently HB-qualified pairs occur at each separation.

HB Strength CDF

To characterize HB geometry, we used TRAVIS's Combined Distribution Function (CDF) analysis, selecting RDF (donor–acceptor distance) as the first function and angular distribution function (ADF) (donor-H···acceptor angle) as the second. This produces a combined distribution P(r,θ) over distance and angle by binning HB events on an (r,θ) grid and normalizing to unit integral. The resulting 2D heat map visualizes the population of HB geometries; high-intensity regions correspond to frequently sampled (short-distance, near-linear) configurations and are used here as a qualitative indicator of stronger hydrogen-bonding geometries. To enable quantitative comparison across systems, the same color scale is applied to all maps.

4.3.3 MSD and self-diffusion coefficients

An important aspect of electrolyte behavior is molecular mobility, which can be quantified through dynamical observables obtained from molecular dynamics simulations. The most widely used descriptor is the mean-square displacement (MSD), which measures how far particles migrate from their initial positions as a function of time. The MSD provides direct information about translational motion and, at sufficiently long times, connects to the self-diffusion coefficient through the Einstein relation.

At very short times, MSDs exhibit a ballistic regime, where motion is dominated by initial velocities and inertia, leading to a quadratic increase with time. At intermediate times, sub-diffusive or caging behavior may appear, particularly in dense liquids or electrolytes, as ions experience temporary trapping by their local environment. Finally, at sufficiently long times, the system reaches the diffusive regime, characterized by a linear MSD growth with time. Only this regime is suitable for extracting diffusion coefficients.

The Einstein relation links the MSD slope in the diffusive regime to the self-diffusion coefficient D:

$$D = \frac{1}{2d} \lim_{t\to\infty} \frac{d}{dt} \langle \frac{1}{N} \sum_{i=1}^{N} |\boldsymbol{r}_i(t) - \boldsymbol{r}_i(0)|^2 \rangle \qquad \textit{Equation 4.7}$$

Here, d is the dimensionality of the system, N is the number of particles included in the average, and the angle brackets denote ensemble or time averaging. The diffusion coefficient is therefore obtained from the slope of the MSD in its long-time linear regime, where ion motions are no longer correlated with their initial environment.

In practice, this calculation requires careful consideration of simulation length: if the production run is too short, MSD curves may not reach a fully diffusive regime, leading to underestimated diffusion values. To ensure reliability, only the portion of MSD curves displaying sustained linearity was used for regression. In **Paper I and II**, the resulting diffusion coefficients were calculated with in-house MATLAB scripts, which processed the raw MSD data, identified the linear regime, and performed least-squares fitting to obtain slopes.

By comparing diffusion constants of cations, anions, and solvent molecules, these analyses provide quantitative insight into the relative mobility of different species. Furthermore, combined with structural analyses (RDF, pCN, HB statistics), diffusion properties contribute to the overall assessment of MLH in the studied electrolytes.

Chapter 5

Results and Discussion

Computational studies play a crucial role in unravelling the relationship between the structure and properties of materials, providing valuable insights that often guide further research investigations. Different computational approaches can be used to simulate DEEs depending on the scale of the electrolyte and the properties to be studied. However, this becomes more challenging because DEEs are complex materials to simulate in comparison to other liquids due to a wider array of intermolecular interactions[92]. Few pathways to study such materials are to use quantum mechanical (QM) methods like DFT to study local DEEs structure in the atomic scale, moving to molecular size with MD simulations, or even thermodynamical modelling through Conductor like Screening Model for Realistic Solvents (COSMO-RS)[93,94] or with excess Gibbs free energy models [95]. Many studies used QM methods to study charge transfer and charge delocalization by resolving the electronic structure [96–98].

As for molecular dynamic simulation, it is more computationally feasible in comparison to DFT, though they provide different information on the molecular interactions of materials and their dynamic properties. Often, MD studies are run in the nanoscale, which provides more statistically sound dynamical descriptions, such as mean square displacement (MSD) and diffusion coefficients. In some cases, DEEs are simulated at their melting temperature and kept constant to ensure a liquid phase if that was the focus; other times, a box would be created with increased temperature and then cooled down again after reaching the melting point. One great challenge in MD simulations revolves around developing force fields that can produce the structural and dynamic characteristics of deep eutectics accurately. The FFs used for DEEs are closely related and based on those of FFs for ionic liquids, given the substantial similarities in their interactions. However, due to differences in their makeup and unique interactions within DEEs, FFs designed for them exhibit distinctive traits. Some central issues arise from the presence of strong ionic interactions and highly polarizable atoms and molecules[92]. Ignoring polarization effects may result in an overestimation of ion-ion interactions [99], potentially yielding unreliable outcomes, such as a drastic reduction in the diffusion

coefficient by several orders of magnitude [99]. Nevertheless, non-polarizable FFs can frequently accurately reproduce the structural features of DEEs [100].

This section provides a summary of the main results of the thesis, drawing on the detailed work presented in **Papers I–V**.

5.1 Local Structure

Local structure in **Papers I, II, IV** is quantified from MD simulations using RDF and CDF/pCN. HB in **Papers I, II** is assessed with HB-distance PDFs for separation distributions and TRAVIS CDF (RDF+ADF) maps as a qualitative indicator of HB strength via joint distance–angle populations.

5.1.1 Effect of anion size and symmetry on Li and Ca DEEs

Intermolecular interactions play a key role in DEEs and understanding the electrolyte's local structure helps us get a better grasp on why DEEs behave this way, molecular ordering and organization and connects to its macroscopic properties. [60,61,101]

Paper I and II local structure analysis based on xTB simulations show the effect of anion size and symmetry affects the hydrogen bonding network which plays a role in molecular-level heterogeneity in DEEs. The lithium salts used in **Paper I** are: $LiBF_4$, LiDFOB, and LiBOB. These salts were selected for their contrasting anionic characteristics: $LiBF_4$ with a pseudospherical BF_4^- geometry lacking oxygen coordination sites, BOB presenting an elongated oxalato-borate with multiple oxygen-rich rings, and DFOB exhibiting intermediate behavior. Building on this, **Paper II** extends the same framework to calcium-based DEEs, incorporating not only $Ca(BF_4)_2$, $Ca(DFOB)_2$, and $Ca(BOB)_2$ electrolytes but also larger, more symmetric anions such as $B(hfip)_2$. The solvent of choice in these two paper was N-methylacetamide (NMA) as a hydrogen bond donor.

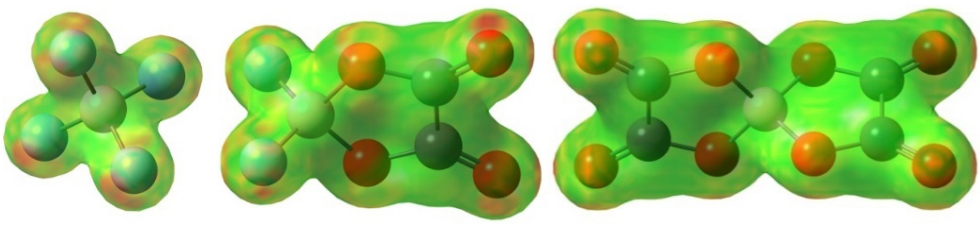

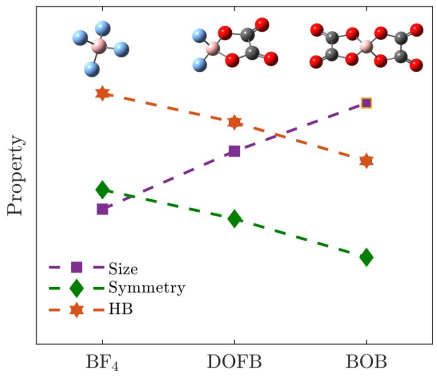

Figure 5.1. Properties of the three anions a) BF4- b) DFOB c) BOB. Top: Electrostatic Potential (ESP) and structures. Bottom: Size, symmetry and HB properties across the anions.

Varying the anion from small, symmetric BF_4^- to bulkier, lower-symmetry DFOB and BOB, shown in Figure 5.1, systematically shifts the first coordination shell contributions from anions and solvent around Li^+. LiBOB exhibits the most ionic association with the highest cation-anion pCN = 2.5. While LiDFOB sits in the middle and $LiBF_4$ shows the weakest pairing with a pCN = 1.4.

Table 5.1. Partial coordination numbers of anion-Solvent of Li-DEEs.

	BF_4		*DFOB*		*BOB*	
	pCN	R (Å)	pCN	R (Å)	pCN	R (Å)
B-N	2.9	4.7	1.2	4.0	0.1	1.9
					0.7	3.9

In parallel, $LiBF_4$ supports the most solvent-rich inner shell: Li–O(NMA) peaks sharply at around ~1.9 Å and integrates to about 2.7 NMA oxygens in the first shell owing to the largest solvent pCN among the three, shown in Figure 5.2. On the other hand, LiDFOB and LiBOB progressively displace solvent as the anion occupies more of Li^+'s inner shell. Within LiDFOB, cation–anion contacts are predominantly oxalate oxygen-based rather than fluorine-based, emphasizing the dominance of the oxalate oxygens in cation coordination.

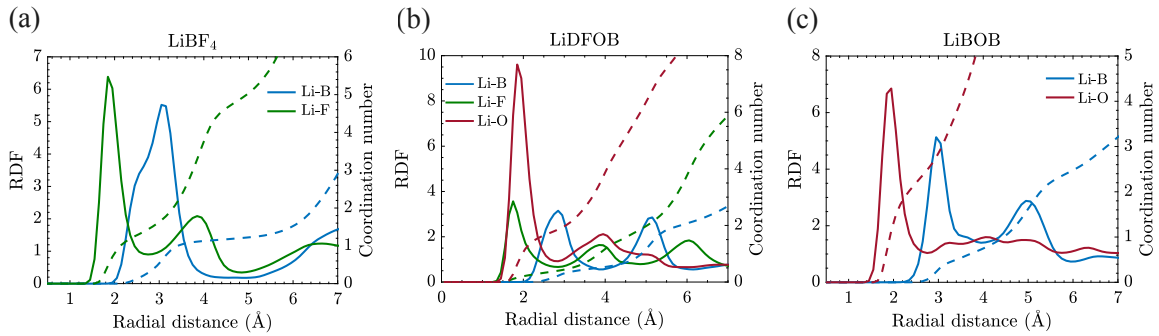

Figure 5.2. RDF showcasing coordination differences across three electrolytes a) LiBF4 b) LiDFOB c) LiBOB.

Anion–solvent coordination mirrors this structural picture: BF_4^- is the most evenly and strongly solvated by NMA (B–N pCN = 2.9), while DFOB is lower and BOB the least, consistent with steric exclusion near large, oxygen-rich rings. Spatially, $LiBF_4$ presents an almost sealed SDF isosurface around the anion (see Fig. 5.3), showcasing a comparatively homogeneous local environment, whereas LiDFOB and especially LiBOB break into more localized, fragmented pockets, meaning a more heterogeneous environment.

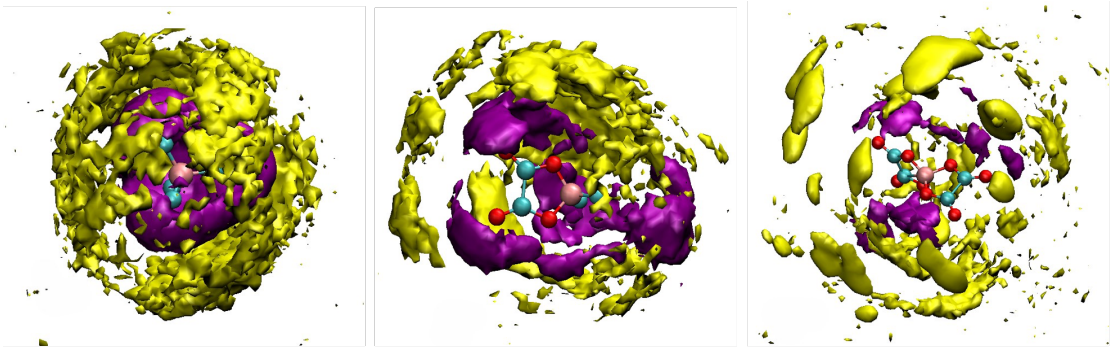

Figure 5.3. SDF of Li-DEEs around the anions (a) LiBF4, (b) LiDFOB, and (c) LiBOB showing lithium in purple and NMA in yellow.

The anion–anion RDF for LiBOB further shows a distinct binodal feature around 4.1 and 5.0 Å visible in Figure 5.4, signaling intermediate-range ordering within anion-rich domains.

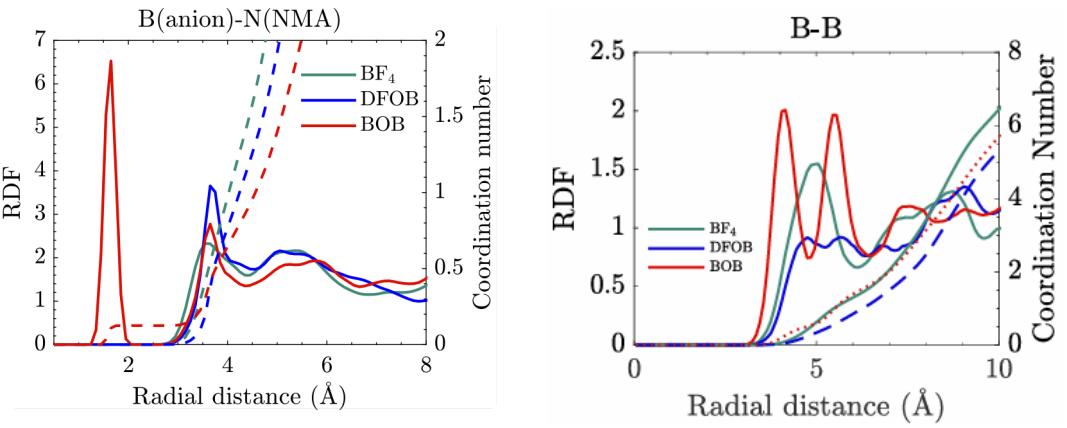

Figure 5.4. RDF of anion-solvent interaction and anion-anion interaction.

Moving to a calcium-based electrolyte in **Paper II**, the qualitative ordering of anion effects is preserved while amplifying overall coordination due to its higher charge and larger coordination number. In $Ca(BF_4)_2$, Ca^{2+} remains largely solvent-separated in the first shell with a Ca-O(NMA) of 3.6 and weak Ca–F showing a broad and low RDF peak (see Fig. 5.5). A spectator NMA can reside within first-shell radii without forming a true Ca–O coordination. In $Ca(DFOB)_2$ and $Ca(BOB)_2$, oxalate oxygens chelate Ca^{2+} directly, displacing solvent and producing mixed inner shells with multiple O donors. $Ca(B(hfip)_4)_2$ is characterized by broad shells and a high count of Ca–F/O contact sites per anion, yet a low number of distinct anions per Ca^{2+} (multidentate binding inflates contact pCNs).

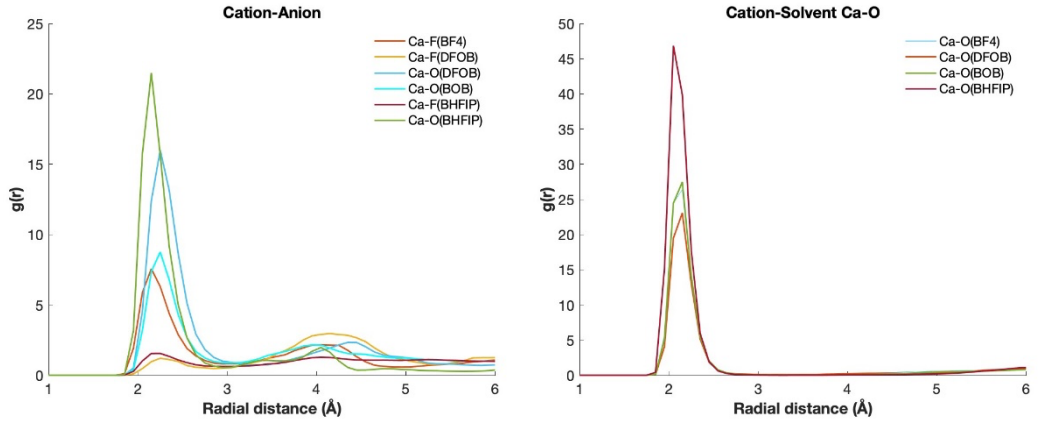

Figure 5.5. RDF of calcium DEEs showing a) cation-anion interaction, b) cation-solvent interaction.

The Ca–B RDFs reinforce this picture: BF_4^- and $B(hfip)_4$ show a near-first-shell signature for B that decays rapidly; BOB signals linger into the second shell; DFOB exhibits multiple farther peaks, indicating more persistent anion presence around Ca^{2+}. Comparing cation–cation and anion–anion ordering with the Li-DEEs, the Ca–Ca RDF peaks appear at slightly longer distances, reflecting the larger cation, yet are spaced more closely, consistent with more compact cation–anion entities. The B–B RDFs reveal that $Ca(BOB)_2$ and $Ca(B(hfip)_4)_2$ exhibit more layered order, with distinct oscillations and minima.

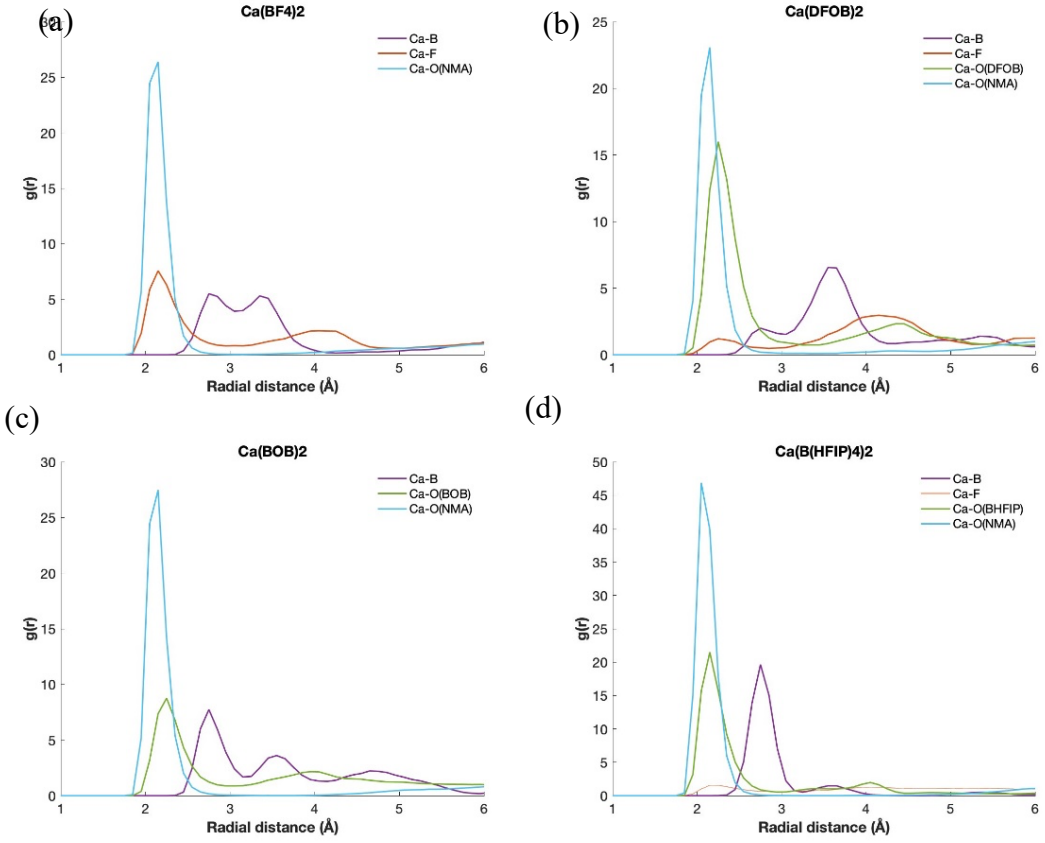

Figure 5.6 RDFs of calcium DEEs a) $Ca(BF_4)_2$ b) $Ca(DFOB)_2$ c) $Ca(BOB)_2$ d) $Ca(B(HFIP)_4)_2$

5.1.2 Hydrogen Bonding

The hydrogen-bond network follows the same steric and symmetry pattern. $LiBF_4$ concentrates strong F···H(NMA) interactions at short range (see Fig. 5.7) and sustains a relatively delocalized HB network through the solvent-rich environment. LiDFOB

preserves robust F···H while adding O···H contributions from oxalate oxygens, yielding a mixed acceptor landscape.

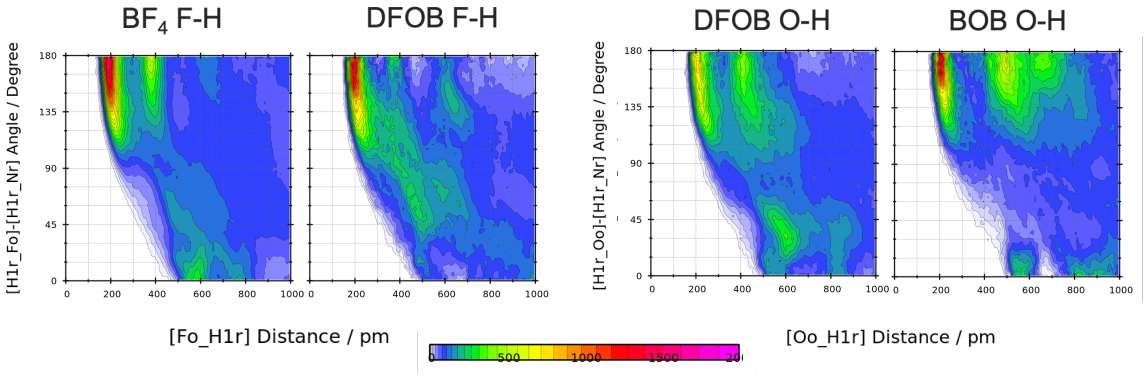

Figure 5.7 HB strength heatmap in lithium DEE.

In LiBOB, steric shadowing near the oxalate rings pushes O···H to longer distances, producing more localized HB bands that align with the anion-rich structural pockets. HB lifetimes reflect this shift: as anions grow bulkier and more O-dominated, the network becomes more persistent locally but less connected globally.

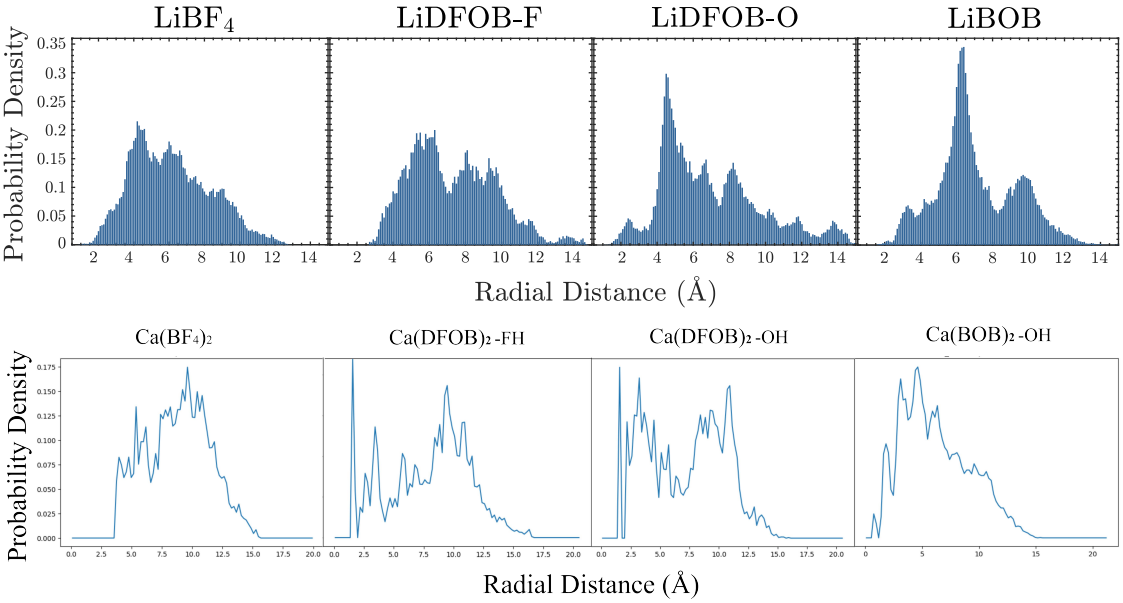

Figure 5.8 HB distribution in lithium DEEs (top) and calcium DEEs (bottom).

Moving from Li^+ to Ca^{2+} decreases the availability of free HB acceptors: oxalate and solvent oxygens are more frequently bound to Ca^{2+}, and HB intensity correspondingly drops and redistributes. The HB CDFs show that $Ca(BF_4)_2$ retains the strongest short-range, near-linear N–H···F domain, $Ca(DFOB)_2$ and $Ca(BOB)_2$ display weaker, more

dispersed HB signatures as Ca–O coordination competes with N–H donation. $Ca(B(hfip)_4)_2$ is HB-poor, with only faint long-range H···F features due to steric shielding of O donors. Overall, the Ca-based DEEs exhibit reduced HB intensity relative to Li-based systems, consistent with more Ca–anion/solvent coordination and with the SDF/RDF picture of more restricted solvent approach around Ca^{2+}.

Table 5.2. Partial coordination numbers of HB pairs in Li and Ca-DEEs.

	$LiBF_4$		**LiDFOB**			**LiBOB**		
Pair	pCN	Distance (Å)	Pair	pCN	Distance (Å)	Pair	pCN	Distance (Å)
F-H	1.2	3.2	F-H	1.3	3.5	O-H	0.5	3.2
			O-H	0.8	3.3			

	$Ca(BF_4)_2$		**$Ca(DFOB)_2$**		**$Ca(BOB)_2$**		**$Ca(B(HFIP)_4)_2$**	
	pCN	R (Å)	pCN	R (Å)	pCN	R (Å)	pCN	R (Å)
F-H	1.3 3.6	3.3 4.7	0.7 10.8	3.2 7.1	-	-	0.2 3.2	3.0 6.0
O-H	-	-	0.5 7.5	3.1 6.4	0.5	3.2	0.1	3.0

5.1.3 Effect of salt concentration on coordination structure in DEEs vs HCEs

In **Paper IV**, Li^+ is only partially coordinated with a pCN ≈ 2.3 for urea and 1.7 for DMU, leaving many solvent molecules 'free' or H-bonded (see Fig.5.9). In more concentrated 1:2 formulations (DMU12, urea12, TDEE111), free solvent is negligible and solvent–solvent H-bonding largely gives way to Li^+–solvent coordination. At equal salt fraction, urea-based DEEs show smaller Li–O(FSA)/Li–F pCNs than DMU-based ones, indicating enhanced ion dissociation, consistent with their higher measured ionicity.

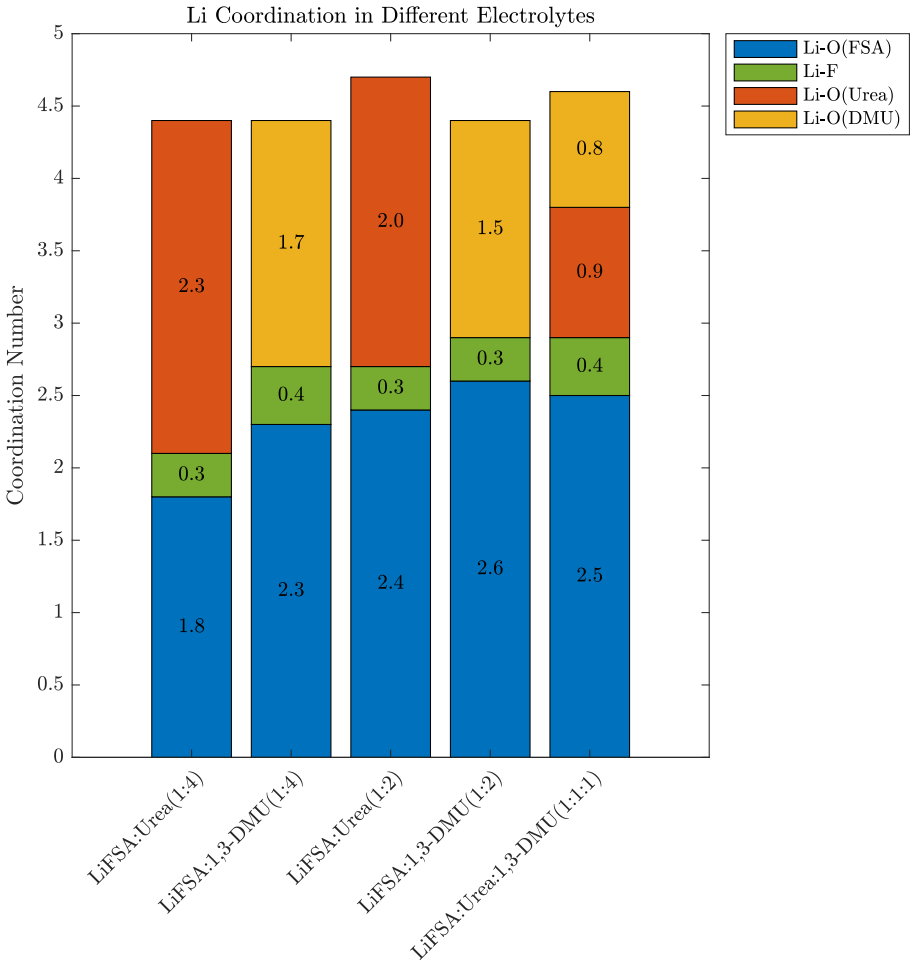

Figure 5.9. pCN of Urea and DMU-based DEE

In NaTFSI–AND in **Paper V**, ADN coordinates Na^+ in an ordered, network-like fashion at ADN-rich composition: at x = 11, the Na total CN within 2.5 Å is 4, and the Na–N(ADN) pCN shows a sharp rise to a plateau shown in Figure 9.10. As TFSI content increases, the ADN plateau decreases, reaching a minimum of 2 at x = 3 (2.9 M), and then increases again at the highest concentration x = 2 (4.4 M). By contrast, Na–TFSI cumulative pCNs increase gradually with concentration (no plateau), indicating a more disordered anion arrangement. At x = 3, distances >3.0 Å are needed to reach CN ≈ 4 (the <2.5 Å plateau seen at x = 11 disappears), while at x = 2, the local coordination changes profoundly. Altogether, this supports a percolating Na^+–ADN network with communal solvation, with TFSI filling free-volume voids at high concentration.

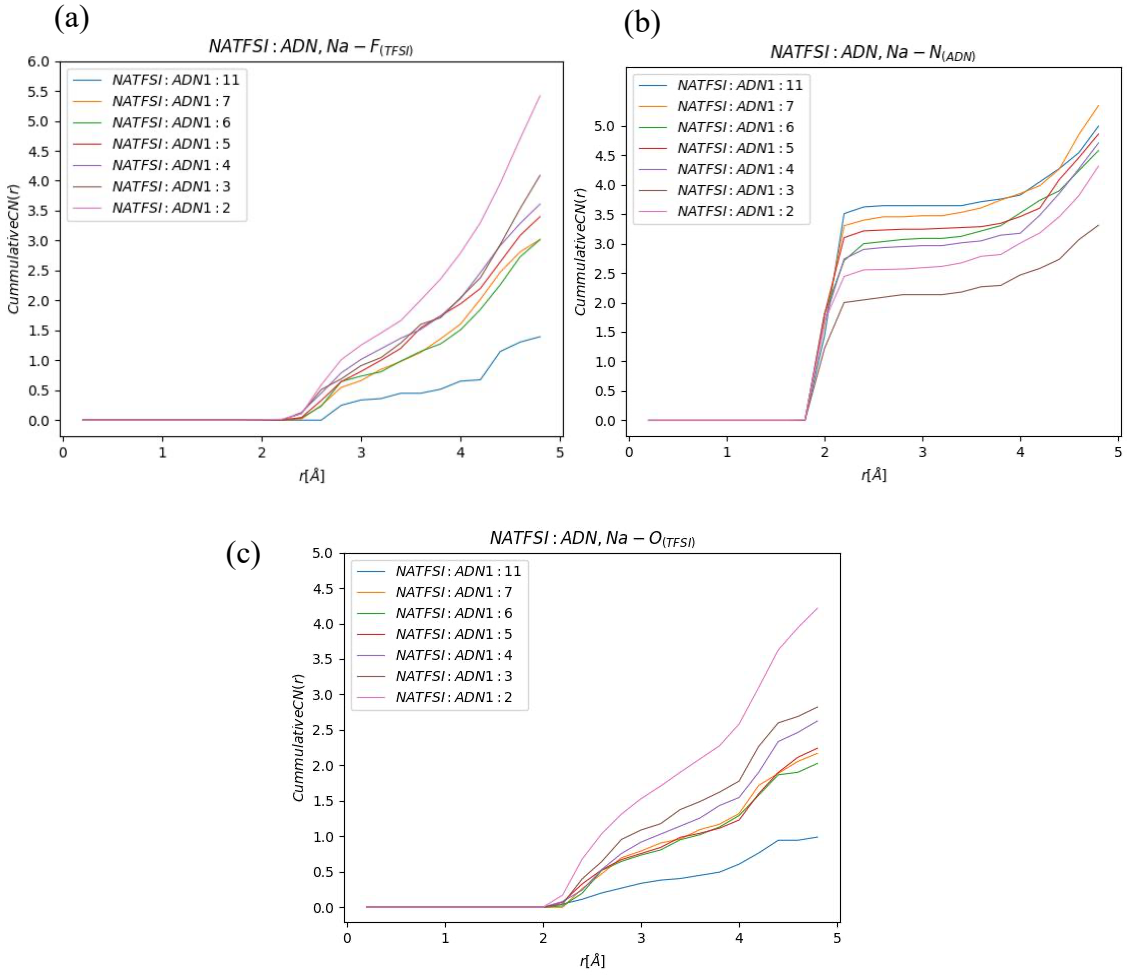

Figure 5.10. Calculated cumulative pCNs for (a) Na-F, (b) Na-N, and (c) Na-O in NaTFSI –ADN.

5.2 Dynamics and Transport Properties

The MSDs and self-diffusion coefficients place $LiBF_4$ as the fastest electrolyte, followed by LiDFOB and then LiBOB, with roughly a two-fold spread across the DEEs. In $LiBF_4$, NMA diffuses fastest, the anion next, and Li^+ slowest, which is consistent with a solvent-rich, weakly correlated environment. In LiDFOB and LiBOB, cation and anion diffusivities move closer together, indicating stronger ion pairing and more correlated motion as the first shell becomes anion-dominated and the HB network tightens. The marked drop in solvent mobility from $LiBF_4$ to LiDFOB, and its further reduction in LiBOB, is consistent with the structural picture: as anions occupy more of lithium's inner shell and hydrogen bonds concentrate locally, the available space and continuity for solvent motion decrease, producing a more constrained electrolyte.

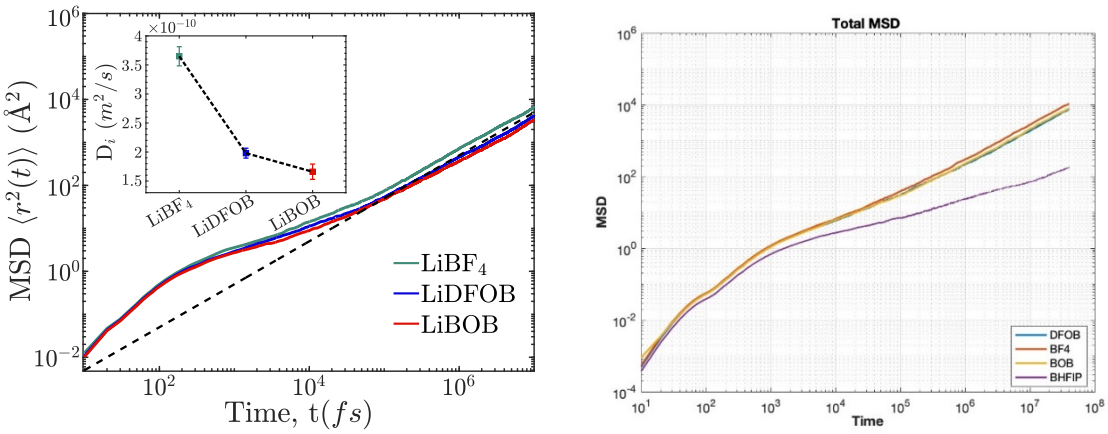

Figure 5.11. . Left: Total MSD of Li-DEEs with a subplot of Diffusion coefficients. Right: Total MSD of Ca-DEEs.

Across the calcium electrolytes, the total MSDs (Fig. 5.12) show the expected shift from an initial ballistic to diffusive regime. The total MSD slopes give the transport order:

$Ca(BF_4)_2 > Ca(DFOB)_2 > Ca(BOB)_2 > Ca(B(hfip)_4)_2$.

Higher total mobility in $Ca(BF_4)_2$ reflects greater solvent accessibility to Ca^{2+} and the presence of short, near-linear HBs (seen in HB CDFs), both of which facilitate molecular rearrangements and motion. In $Ca(DFOB)_2$ and $Ca(BOB)_2$, stronger Ca–anion coordination limits solvent approach and lowers total mobility. $Ca(B(hfip)_4)_2$ exhibits the lowest total mobility, consistent with a tightly filled Ca^{2+} coordination environment and reduced HB participation, conditions that constrain molecular motion on longer timescales.

5.3 Molecular-Level Heterogeneity in DEEs

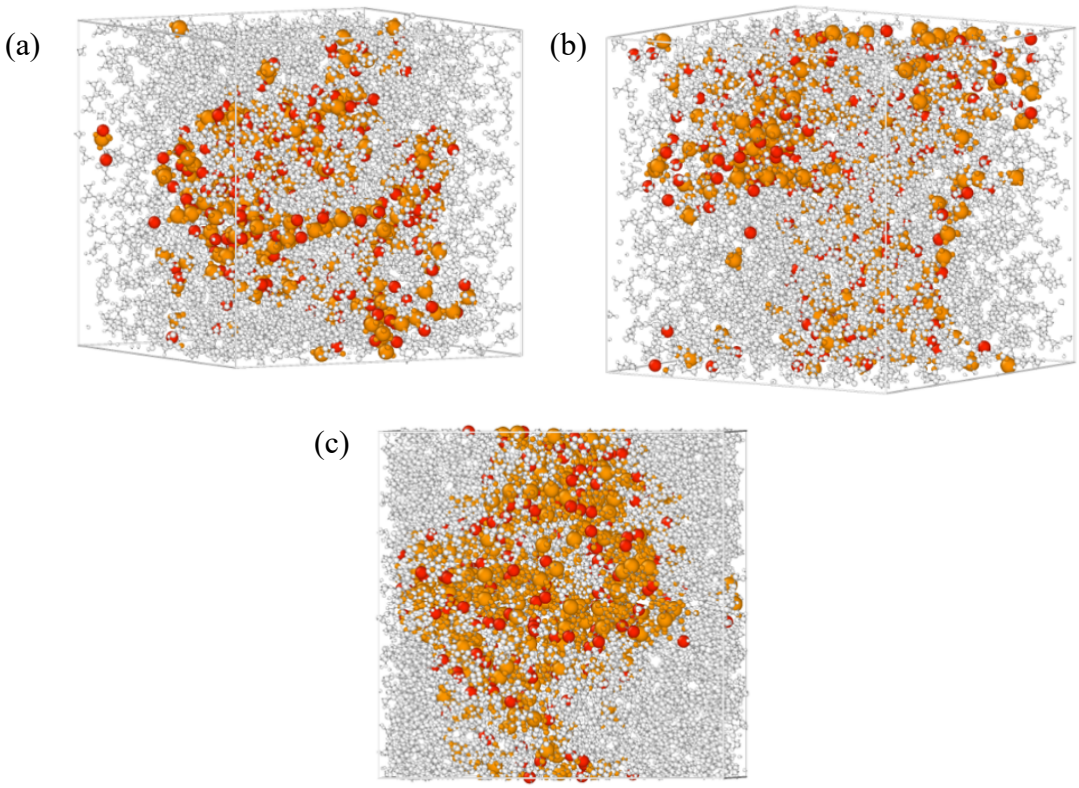

Figure 5.2.6. Screenshots from MD production simulation showing lithium in red, anion in orange and NMA in white for a) LiBF4 b) LiDFOB c) LiBOB

Utilizing different analyses together in **Papers I and II**, such as RDF/pCN trends, SDF, HB distributions, and diffusion ordering, helps us understand the heterogeneity variation in these DEEs. $LiBF_4$ is the most homogeneous, with a nearly isotropic local solvation environment and more delocalized HBs; LiBOB is the most heterogeneous, showing anisotropic anion-rich regions and more localized HB zones; LiDFOB falls between, combining oxygen- dominant cation binding with residual F engagement. A composite

MLH index built from these metrics using HB localization, diffusion ratios, solvation numbers, and anion size/symmetry, reproduces this order and shows how each descriptor contributes to the final score.

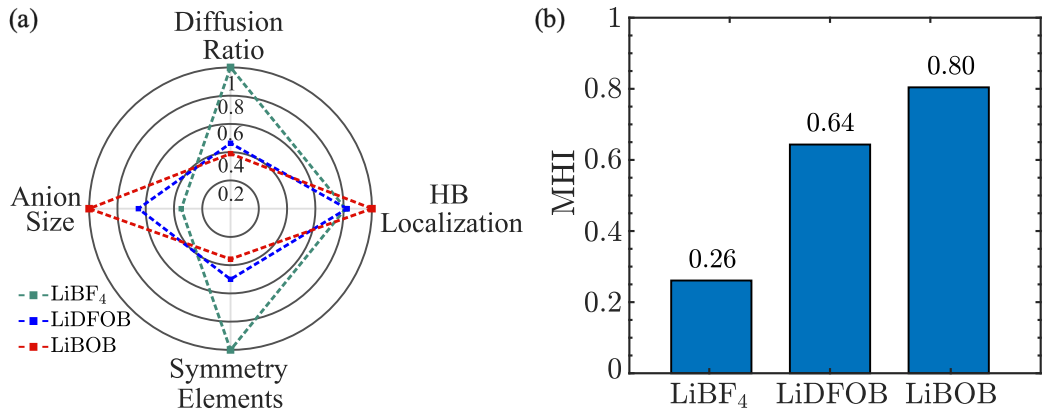

Figure 5.2.7. MLH index score across the three Li-DEEs.

Moving to calcium-DEEs changes the MLH patterns slightly compared to Li-DEEs. The divalent cation and multidentate Ca–O coordination increase competition for binding sites, reduce freely available HB contacts, and raise heterogeneity relative to the Li-DEEs (see Fig. 5.2.8). $Ca(BF_4)_2$ remains comparatively uniform and isotropic; $Ca(DFOB)_2$ and $Ca(BOB)_2$ display more fragmented, competitive local environments with more prevalent ionic association. $Ca(B(hfip)_4)_2$ represents the upper bound, with more persistent Ca–anion coordination, minimal HB participation, and anisotropic ion-rich regions that limit solvent integration and supresses transport.

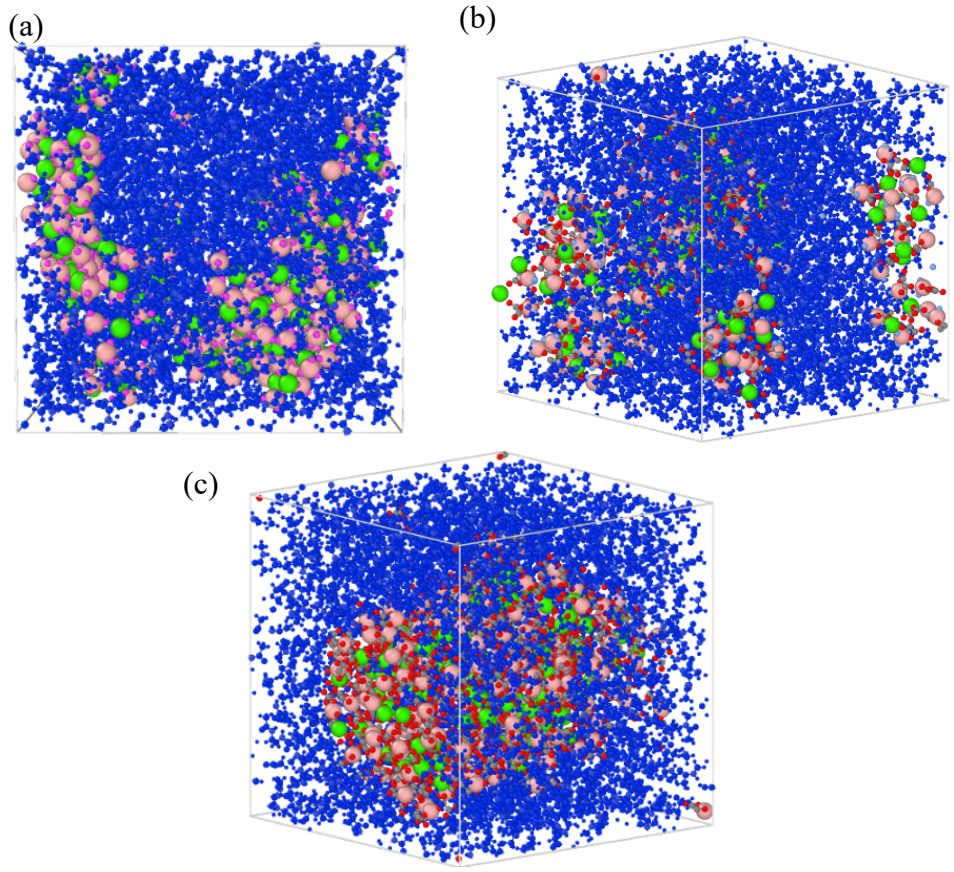

Figure 5.2.8. Screenshots from MD production simulation showing calcium in green, anion in pink and NMA in red for a) $Ca(BF_4)_2$ b) $Ca(DFOB)_2$ c) $Ca(BOB)_2$

Chapter 6

Conclusions and Outlook

Liquid electrolytes sit at the heart of modern batteries. They enable performance, but they also set the limits, stability windows, transport, and lifetime. What needs further study is a clear link between materials' macroscopic properties and the molecular scale, especially in DEEs and related concentrated electrolytes. This thesis attempts to bridge that by connecting molecular structure and dynamics to macroscopic behaviour through MD simulations, using SQM methods where they offer a practical balance between accuracy and speed, and cross-checking with experiments when possible.

Papers I and II set the main thread. A comprehensive computational analysis examines how anion size and symmetry affect HB and MLH, and how these changes carry through to electrolyte properties. The same framework is then extended from lithium to calcium. Calcium offers promise for sustainability and performance, even though the technology remains early, and the same structure-to-property logic helps identify realistic directions. **Paper IV** uses MD to clarify lithium coordination and changes in solvation shells in urea- and 1,3-dimethylurea-based DEEs over different concentrations, which helps explain the observed macroscopic trends. **Paper V** explores sodium salt in ADN across a wide concentration range, where simulations and measurements together indicate network formation and glass-like features at higher concentration, consistent with the observed stability window.

Looking ahead, several steps would strengthen both this contribution and the wider field. Quantitative heterogeneity could be turned into a predictive measure for transport and stability. Beyond first-shell statistics, cluster size, shape, lifetime, and self-diffusion can be extracted and linked to collective diffusion and conductivity. Percolation analysis can determine whether aggregates connect into system-spanning pathways or remain as separate islands, and how each regime correlates with viscosity, transference number, and desolvation kinetics. For the urea DEE study, an extended molecular-level analysis of HB network topology and species self-diffusion would provide a more rounded view

of how composition tunes dissociation, clustering, and mobility, and where a workable balance lies between stability and excess structuring.

For calcium DEEs, it would be useful to complement molecular and electrochemical studies with life cycle assessment, to test whether sustainability claims hold once precursor sourcing, processing energy, and end of life are counted, and to prioritise chemistries that make sense both technically and environmentally. It would also be valuable to complement this with experimental work by synthesising and testing the DEEs proposed in Papers I and II, linking the molecular picture to measurable cell performance.

The use of different methods should align to be useful, and bridging experimental and computational work remains essential. No single technique is more accurate in the abstract, since each resolves a different facet of the material. The most reliable understanding emerges when observables are made comparable, definitions are precise, and results are assembled so they fit together like a puzzle. In this way, we can “see the whole elephant” rather than isolated parts.

Ultimately, it is wise to optimise how existing data are interpreted and to treat coordination and heterogeneity in DEEs as tunable design variables, enabling rational, scalable electrolyte design across next-generation lithium and calcium electrolytes.

Acknowledgments

I would like to begin by thanking my supervisor, Patrik Johansson, whose support and encouragement allowed me to explore ideas and imagination in research. Thank you for your mentorship and for helping me grow as a researcher. I also thank my examiner, Aleksandar Matic, for embracing and sometimes even supporting my random ideas, such as creating matching running shirts for MF, although an MF dog visit or goat yoga are still valid ideas..

A special thanks to my former and current officemates, your warmth and spontaneous conversations enriched my time here. I'm especially grateful to Linnea for her friendship and wisdom: for listening patiently to my wild stories and thoughts, and then always offering something logical to bring me back to reality. I'm also grateful to my conference travel buddies, Carolina and Johanna, for the fun times and endless pseudo-therapy sessions.

I am grateful to Patricia and Zaher for their help with drafts, insightful comments, and consistent support, and thankful to Ezio for his technical support. I would like to thank Magnus Karlsteen, one of the best educators I know. Thank you for supporting my dreams and being a source of light and a pillar for students.

I am very grateful to the MF division and all its members for countless engaging conversations, shared moments, and the warmth of fikas and food sharing that brightened my days. I'm also grateful for MF members, current and past, including Soniya, one of the two people who witnessed my hiker girl era, Laura who always comes with a calm sigh and "Oh Mirna" after I spill all the weird in my day at 1.5x speed, and Leonard, a fellow linguistics and history geek and a kind soul.

I'm also grateful to everyone at Chalmers who brightened my days, from fika conversations with Ageo to lunch dates with Esmee and countless small kindnesses.

To my amazing power girls in Physics: Pantea, Emelie, Kajsa, Ariadna, Laura, and many more. You are some of the smartest and strongest women I've met. I can't wait to see the great things you'll achieve. Thank you for the strong support and conversations; you helped keep my sanity and my spirits high.

To my American family, the Bloomers and the Tooleys, thank you for carrying me through my bachelor's years. I miss you today and wish you were here.

Living across the continents has been a joy and also a bittersweet pull. To friends spread across the world, from east to west and all in between: I'm thinking of you today; your friendship has meant the world.

Lastly, my heartfelt thanks go to my family for their unwavering support, especially Rima and Mom, who took such good care of me while I cared for this thesis, who gently forced me out on nature hikes when I was stressed, and who humored my late-night randomness, from political and philosophical debates to hearing me obsess about the magical party venue of my dreams. To my amazing family and friends: you are my safe place and steady anchor; thank you, too, for putting up with far too many of my dad jokes. Most of all, to my dad, Deeb, the visionary, who kept sending me articles of scientific breakthroughs in battery materials even before I decided to pursue this PhD, and who never got to see it completed, I dedicate this to you.

Bibliography

(1) Fleischmann, J.; Hanicke, M.; Horetsky, E.; Ibrahim, D.; Jautelat, S.; Linder, M.; Schaufuss, P.; Torsch, L.; van de Rijt, A. *Battery 2030: Resilient, Sustainable, and Circular*; 2023.

(2) Blomgren, G. E. The Development and Future of Lithium Ion Batteries. *J. Electrochem. Soc.* **2017**, *164* (1), A5019–A5025. https://doi.org/10.1149/2.0251701jes.

(3) Petit, S.; Vafeas, A.; Coujard, C. *Battery Energy Storage Systems to Support the Large-Scale Integration of Renewable Energy (BRIDGE Case Study No. 3)*; European Commission Directorate-General for Energy, 2022. https://bridge-smart-grid-storage-systems-digital-projects.ec.europa.eu/sites/default/files/case-studies/03_BESS_Case%20study_v2.pdf.

(4) Kim, J.-S.; Song, J.-S.; Kim, C.-H.; Mahseredjian, J.; Kim, S.-H. Consideration on Present and Future of Battery Energy Storage System to Unlock Battery Value. *J. Mod. Power Syst. Clean Energy* **2024**, *13* (2), 622–636. https://doi.org/10.35833/mpce.2023.000723.

(5) Wei, Q.; Zhang, L.; Sun, X.; Liu, T. L. Progress and Prospects of Electrolyte Chemistry of Calcium Batteries. *Chem. Sci.* **2022**, *13* (20), 5797–5812. https://doi.org/10.1039/D2SC00267A.

(6) Whittingham, M. S. Lithium Batteries and Cathode Materials. *Chem. Rev.* **2004**, *104* (10), 4271–4302. https://doi.org/10.1021/cr020731c.

(7) Goodenough, J. B.; Park, K.-S. The Li-Ion Rechargeable Battery: A Perspective. *J. Am. Chem. Soc.* **2013**, *135* (4), 1167–1176. https://doi.org/10.1021/ja3091438.

(8) Cheng, X.-B.; Zhang, R.; Zhao, C.-Z.; Zhang, Q. Toward Safe Lithium Metal Anode in Rechargeable Batteries: A Review. *Chem. Rev.* **2017**, *117* (15), 10403–10473. https://doi.org/10.1021/acs.chemrev.7b00115.

(9) Yu, Z.; Rudnicki, P. E.; Zhang, Z.; Huang, Z.; Celik, H.; Oyakhire, S. T.; Chen, Y.; Kong, X.; Kim, S. C.; Xiao, X.; Wang, H.; Zheng, Y.; Kamat, G. A.; Kim, M. S.; Bent, S. F.; Qin, J.; Cui, Y.; Bao, Z. Rational Solvent Molecule Tuning for High-Performance Lithium Metal Battery Electrolytes. *Nat. Energy* **2022**, *7* (1), 94–106. https://doi.org/10.1038/s41560-021-00962-y.

(10) Li, Y.; Ni, Z.; Geng, J.; Wang, Z.; Li, Y.; Zhao, Y.; Shao, H.; Li, Y.; Xiong, S.; Feng, J. Advancements in Electrolytes: From Liquid to Solid for Low-Cost and High-Energy-Density Micro-Sized Silicon-Based Batteries. *Adv. Energy Mater.* **2025**. https://doi.org/10.1002/aenm.202502284.

(11) Lithium Metal Stabilization for Next-Generation Lithium-Based Batteries: From Fundamental Chemistry to Advanced Characterization and Effective Protection. *Energy Mater.* **2023**, *3* (1), 300002. https://doi.org/10.20517/energymater.2022.60.

(12) Ren, X.; Zou, L.; Jiao, S.; Mei, D.; Engelhard, M. H.; Li, Q.; Lee, H.; Niu, C.; Adams, B. D.; Wang, C.; Liu, J.; Zhang, J.-G.; Xu, W. High-Concentration Ether Electrolytes for Stable High-Voltage Lithium Metal Batteries. *ACS Energy Lett.* **2019**, *4* (4), 896–902. https://doi.org/10.1021/acsenergylett.9b00381.

(13) Hu, G.; Yang, Z.; Zhang, X.; Liu, Y.; Lin, Y.; Chen, S.; Chen, Y.; Sa, B.; Zhang, Y. Strongly Solvating Triglyme-Based Electrolyte Realizes Stable Lithium Metal Batteries at High-Voltage and High-Temperature. *Energy Storage Mater.* **2024**, *69*, 103402. https://doi.org/10.1016/j.ensm.2024.103402.

(14) Chen, Y.; Li, M.; Liu, Y.; Jie, Y.; Li, W.; Huang, F.; Li, X.; He, Z.; Ren, X.; Chen, Y.; Meng, X.; Cheng, T.; Gu, M.; Jiao, S.; Cao, R. Origin of Dendrite-Free Lithium Deposition in Concentrated Electrolytes. *Nat. Commun.* **2023**, *14* (1). https://doi.org/10.1038/s41467-023-38387-8.

(15) Bannwarth, C.; Ehlert, S.; Grimme, S. GFN2-xTB—An Accurate and Broadly Parametrized Self-Consistent Tight-Binding Quantum Chemical Method with Multipole Electrostatics and Density-Dependent Dispersion Contributions. *J. Chem. Theory Comput.* **2019**, *15* (3), 1652–1671. https://doi.org/10.1021/acs.jctc.8b01176.

(16) *LITHIUM-ION BATTERIES." Nobel Prize*; The Royal Swedish Academy of Sciences, 2019. www.nobelprize.org/uploads/2019/10/advanced-chemistryprize2019.pdf.

(17) Jiao, S.; Ren, X.; Cao, R.; Engelhard, M. H.; Liu, Y.; Hu, D.; Mei, D.; Zheng, J.; Zhao, W.; Li, Q.; Liu, N.; Adams, B. D.; Ma, C.; Liu, J.; Zhang, J.-G.; Xu, W. Stable Cycling of High-Voltage Lithium Metal Batteries in Ether Electrolytes. *Nat. Energy* **2018**, *3* (9), 739–746. https://doi.org/10.1038/s41560-018-0199-8.

(18) Hu, Z.; Xian, F.; Guo, Z.; Lu, C.; Du, X.; Cheng, X.; Zhang, S.; Dong, S.; Cui, G.; Chen, L. Nonflammable Nitrile Deep Eutectic Electrolyte Enables High-Voltage Lithium Metal Batteries. *Chem. Mater.* **2020**, *32* (8), 3405–3413. https://doi.org/10.1021/acs.chemmater.9b05003.

(19) Chen, S.; Zheng, J.; Yu, L.; Ren, X.; Engelhard, M. H.; Niu, C.; Lee, H.; Xu, W.; Xiao, J.; Liu, J.; Zhang, J.-G. High-Efficiency Lithium Metal Batteries with Fire-Retardant Electrolytes. *Joule* **2018**, *2* (8), 1548–1558. https://doi.org/10.1016/j.joule.2018.05.002.

(20) Jaumaux, P.; Liu, Q.; Zhou, D.; Xu, X.; Wang, T.; Wang, Y.; Kang, F.; Li, B.; Wang, G. Deep-Eutectic-Solvent-Based Self-Healing Polymer Electrolyte for Safe and Long-Life Lithium-Metal Batteries. *Angew. Chem. Int. Ed.* **2020**, *59* (23), 9134–9142. https://doi.org/10.1002/anie.202001793.

(21) Ferrari, S.; Falco, M.; Muñoz-García, A. B.; Bonomo, M.; Brutti, S.; Pavone, M.; Gerbaldi, C. Solid-State Post Li Metal Ion Batteries: A Sustainable Forthcoming Reality? *Adv. Energy Mater.* **2021**, *11* (43), 2100785. https://doi.org/10.1002/aenm.202100785.

(22) Dunn, B.; Kamath, H.; Tarascon, J.-M. Electrical Energy Storage for the Grid: A Battery of Choices. *Science* **2011**, *334* (6058), 928–935. https://doi.org/10.1126/science.1212741.

(23) Soloveichik, G. L. Battery Technologies for Large-Scale Stationary Energy Storage. *Annu. Rev. Chem. Biomol. Eng.* **2011**, *2* (1), 503–527. https://doi.org/10.1146/annurev-chembioeng-061010-114116.

(24) Zhang, J.; Yao, X.; Misra, R. K.; Cai, Q.; Zhao, Y. Progress in Electrolytes for Beyond-Lithium-Ion Batteries. *J. Mater. Sci. Technol.* **2020**, *44*, 237–257. https://doi.org/10.1016/j.jmst.2020.01.017.

(25) Hwang, J.-Y.; Myung, S.-T.; Sun, Y.-K. Sodium-Ion Batteries: Present and Future. *Chem. Soc. Rev.* **2017**, *46* (12), 3529–3614. https://doi.org/10.1039/C6CS00776G.

(26) Vaalma, C.; Buchholz, D.; Weil, M.; Passerini, S. A Cost and Resource Analysis of Sodium-Ion Batteries. *Nat. Rev. Mater.* **2018**, *3* (4), 18013. https://doi.org/10.1038/natrevmats.2018.13.

(27) Yoo, H. D.; Shterenberg, I.; Gofer, Y.; Gershinsky, G.; Pour, N.; Aurbach, D. Mg Rechargeable Batteries: An on-Going Challenge. *Energy Environ. Sci.* **2013**, *6* (8), 2265. https://doi.org/10.1039/c3ee40871j.

(28) Muldoon, J.; Bucur, C. B.; Gregory, T. Quest for Nonaqueous Multivalent Secondary Batteries: Magnesium and Beyond. *Chem. Rev.* **2014**, *114* (23), 11683–11720. https://doi.org/10.1021/cr500049y.

(29) Ponrouch, A.; Frontera, C.; Bardé, F.; Palacín, M. R. Towards a Calcium-Based Rechargeable Battery. *Nat. Mater.* **2016**, *15* (2), 169–172. https://doi.org/10.1038/nmat4462.

(30) Armand, M.; Axmann, P.; Bresser, D.; Copley, M.; Edström, K.; Ekberg, C.; Guyomard, D.; Lestriez, B.; Novák, P.; Petranikova, M.; Porcher, W.; Trabesinger, S.; Wohlfahrt-Mehrens, M.; Zhang, H. Lithium-Ion Batteries – Current State of the Art and Anticipated Developments. *J. Power Sources* **2020**, *479*, 228708. https://doi.org/10.1016/j.jpowsour.2020.228708.

(31) Li, M.; Lu, J.; Ji, X.; Li, Y.; Shao, Y.; Chen, Z.; Zhong, C.; Amine, K. Design Strategies for Nonaqueous Multivalent-Ion and Monovalent-Ion Battery Anodes. *Nat. Rev. Mater.* **2020**, *5* (4), 276–294. https://doi.org/10.1038/s41578-019-0166-4.

(32) Canepa, P.; Sai Gautam, G.; Hannah, D. C.; Malik, R.; Liu, M.; Gallagher, K. G.; Persson, K. A.; Ceder, G. Odyssey of Multivalent Cathode Materials: Open Questions

and Future Challenges. *Chem. Rev.* **2017**, *117* (5), 4287–4341. https://doi.org/10.1021/acs.chemrev.6b00614.

(33) Zhang, H.; Qiao, L.; Kühnle, H.; Figgemeier, E.; Armand, M.; Eshetu, G. G. From Lithium to Emerging Mono- and Multivalent-Cation-Based Rechargeable Batteries: Non-Aqueous Organic Electrolyte and Interphase Perspectives. *Energy Environ. Sci.* **2023**, *16* (1), 11–52. https://doi.org/10.1039/D2EE02998G.

(34) Arroyo-de Dompablo, M. E.; Ponrouch, A.; Johansson, P.; Palacín, M. R. Achievements, Challenges, and Prospects of Calcium Batteries. *Chem. Rev.* **2020**, *120* (14), 6331–6357. https://doi.org/10.1021/acs.chemrev.9b00339.

(35) Shakourian-Fard, M.; Kamath, G.; Taimoory, S. M.; Trant, J. F. Calcium-Ion Batteries: Identifying Ideal Electrolytes for Next-Generation Energy Storage Using Computational Analysis. *J. Phys. Chem. C* **2019**, *123* (26), 15885–15896. https://doi.org/10.1021/acs.jpcc.9b01655.

(36) Stievano, L.; De Meatza, I.; Bitenc, J.; Cavallo, C.; Brutti, S.; Navarra, M. A. Emerging Calcium Batteries. *J. Power Sources* **2021**, *482*, 228875. https://doi.org/10.1016/j.jpowsour.2020.228875.

(37) Yamada, Y.; Yamada, A. Review—Superconcentrated Electrolytes for Lithium Batteries. *J. Electrochem. Soc.* **2015**, *162* (14), A2406. https://doi.org/10.1149/2.0041514jes.

(38) Jiang, G.; Li, F.; Wang, H.; Wu, M.; Qi, S.; Liu, X.; Yang, S.; Ma, J. Perspective on High-Concentration Electrolytes for Lithium Metal Batteries. *Small Struct.* **2021**, *2* (5), 2000122. https://doi.org/10.1002/sstr.202000122.

(39) Krämer, S.; Weintz, D.; Winter, M.; Cekic-Laskovic, I.; Grünebaum, M. Importance of High-Concentration Electrolytes for Lithium-Based Batteries. *Encyclopedia* **2025**, *5* (1), 20. https://doi.org/10.3390/encyclopedia5010020.

(40) Yamada, Y.; Takazawa, Y.; Miyazaki, K.; Abe, T. Electrochemical Lithium Intercalation into Graphite in Dimethyl Sulfoxide-Based Electrolytes: Effect of Solvation Structure of Lithium Ion. *J. Phys. Chem. C* **2010**, *114* (26), 11680–11685. https://doi.org/10.1021/jp1037427.

(41) Gebbie, M. A.; Smith, A. M.; Dobbs, H. A.; Lee, A. A.; Warr, G. G.; Banquy, X.; Valtiner, M.; Rutland, M. W.; Israelachvili, J. N.; Perkin, S.; Atkin, R. Long Range Electrostatic Forces in Ionic Liquids. *Chem. Commun.* **2017**, *53* (7), 1214–1224. https://doi.org/10.1039/C6CC08820A.

(42) MacFarlane, D. R.; Chong, A. L.; Forsyth, M.; Kar, M.; Vijayaraghavan, R.; Somers, A.; Pringle, J. M. New Dimensions in Salt–Solvent Mixtures: A 4th Evolution of Ionic Liquids. *Faraday Discuss.* **2018**, *206*, 9–28. https://doi.org/10.1039/C7FD00189D.

(43) Yamada, Y.; Furukawa, K.; Sodeyama, K.; Kikuchi, K.; Yaegashi, M.; Tateyama, Y.; Yamada, A. Unusual Stability of Acetonitrile-Based Superconcentrated Electrolytes for Fast-Charging Lithium-Ion Batteries. *J. Am. Chem. Soc.* **2014**, *136* (13), 5039–5046. https://doi.org/10.1021/ja412807w.

(44) Petibon, R.; Aiken, C. P.; Ma, L.; Xiong, D.; Dahn, J. R. The Use of Ethyl Acetate as a Sole Solvent in Highly Concentrated Electrolyte for Li-Ion Batteries. *Electrochimica Acta* **2015**, *154*, 287–293. https://doi.org/10.1016/j.electacta.2014.12.093.

(45) McOwen, D. W.; Seo, D. M.; Borodin, O.; Vatamanu, J.; Boyle, P. D.; Henderson, W. A. Concentrated Electrolytes: Decrypting Electrolyte Properties and Reassessing Al Corrosion Mechanisms. *Energy Env. Sci* **2014**, *7* (1), 416–426. https://doi.org/10.1039/C3EE42351D.

(46) Yamada, Y.; Wang, J.; Ko, S.; Watanabe, E.; Yamada, A. Advances and Issues in Developing Salt-Concentrated Battery Electrolytes. *Nat. Energy* **2019**, *4* (4), 269–280. https://doi.org/10.1038/s41560-019-0336-z.

(47) Yoshida, K.; Nakamura, M.; Kazue, Y.; Tachikawa, N.; Tsuzuki, S.; Seki, S.; Dokko, K.; Watanabe, M. Oxidative-Stability Enhancement and Charge Transport Mechanism in Glyme–Lithium Salt Equimolar Complexes. *J. Am. Chem. Soc.* **2011**, *133* (33), 13121–13129. https://doi.org/10.1021/ja203983r.

(48) Dokko, K.; Tachikawa, N.; Yamauchi, K.; Tsuchiya, M.; Yamazaki, A.; Takashima, E.; Park, J.-W.; Ueno, K.; Seki, S.; Serizawa, N.; Watanabe, M. Solvate Ionic Liquid Electrolyte for Li–S Batteries. *J. Electrochem. Soc.* **2013**, *160* (8), A1304–A1310. https://doi.org/10.1149/2.111308jes.

(49) Ueno, K.; Park, J.-W.; Yamazaki, A.; Mandai, T.; Tachikawa, N.; Dokko, K.; Watanabe, M. Anionic Effects on Solvate Ionic Liquid Electrolytes in Rechargeable Lithium–Sulfur Batteries. *J. Phys. Chem. C* **2013**, *117* (40), 20509–20516. https://doi.org/10.1021/jp407158y.

(50) Borodin, O.; Han, S.-D.; Daubert, J. S.; Seo, D. M.; Yun, S.-H.; Henderson, W. A. Electrolyte Solvation and Ionic Association: VI. Acetonitrile-Lithium Salt Mixtures: Highly Associated Salts Revisited. *J. Electrochem. Soc.* **2015**, *162* (4), A501–A510. https://doi.org/10.1149/2.0891503jes.

(51) Wu, Z.; Liu, H.; Holoubek, J.; Anderson, C.; Shi, L.; Khemchandani, H.; Lu, D.; Liu, D.; Niu, C.; Xiao, J.; Liu, P. The Role of Ion Transport in the Failure of High Areal Capacity Li Metal Batteries. *ACS Energy Lett.* **2022**, *7* (8), 2701–2710. https://doi.org/10.1021/acsenergylett.2c01114.

(52) Zhang, X.; Zou, L.; Xu, Y.; Cao, X.; Engelhard, M. H.; Matthews, B. E.; Zhong, L.; Wu, H.; Jia, H.; Ren, X.; Gao, P.; Chen, Z.; Qin, Y.; Kompella, C.; Arey, B. W.; Li, J.; Wang, D.; Wang, C.; Zhang, J.; Xu, W. Advanced Electrolytes for Fast-Charging

High-Voltage Lithium-Ion Batteries in Wide-Temperature Range. *Adv. Energy Mater.* **2020**, *10* (22), 2000368. https://doi.org/10.1002/aenm.202000368.

(53) Chen, X.; Yu, H. A Computational Review on Localized High-Concentration Electrolytes in Lithium Batteries. *ChemElectroChem* **2024**, *11* (23), e202400444. https://doi.org/10.1002/celc.202400444.

(54) Zheng, T.; Xu, T.; Xiong, J.; Xie, W.; Wu, M.; Yu, Y.; Xu, Z.; Liang, Y.; Liao, C.; Dong, X.; Xia, Y.; Cheng, Y.; Xia, Y.; Müller-Buschbaum, P. Multipoint Anionic Bridge: Asymmetric Solvation Structure Improves the Stability of Lithium-Ion Batteries. *Adv. Sci.* **2024**, *11* (48), 2410329. https://doi.org/10.1002/advs.202410329.

(55) Martin, P.; Årén, F.; Johansson, P. (Localized) Highly Concentrated Electrolytes for Calcium Batteries. *Batter. Supercaps* **2023**, *6* (5), e202300003. https://doi.org/10.1002/batt.202300003.

(56) Abbott, A. P.; Capper, G.; Davies, D. L.; Rasheed, R. K.; Tambyrajah, V. Novel Solvent Properties of Choline Chloride/Urea mixturesElectronic Supplementary Information (ESI) Available: Spectroscopic Data. See Http://Www.Rsc.Org/Suppdata/Cc/B2/B210714g/. *Chem. Commun.* **2003**, No. 1, 70–71. https://doi.org/10.1039/b210714g.

(57) Di Pietro, M. E.; Mele, A. Deep Eutectics and Analogues as Electrolytes in Batteries. *J. Mol. Liq.* **2021**, *338*, 116597. https://doi.org/10.1016/j.molliq.2021.116597.

(58) Boisset, A.; Menne, S.; Jacquemin, J.; Balducci, A.; Anouti, M. Deep Eutectic Solvents Based on N-Methylacetamide and a Lithium Salt as Suitable Electrolytes for Lithium-Ion Batteries. *Phys. Chem. Chem. Phys.* **2013**, *15* (46), 20054. https://doi.org/10.1039/c3cp53406e.

(59) Song, J.; Si, Y.; Guo, W.; Wang, D.; Fu, Y. Organosulfide-Based Deep Eutectic Electrolyte for Lithium Batteries. *Angew. Chem.* **2021**, *133* (18), 9969–9973. https://doi.org/10.1002/ange.202016875.

(60) Abbott, A. P. Deep Eutectic Solvents and Their Application in Electrochemistry. *Curr. Opin. Green Sustain. Chem.* **2022**, *36*, 100649. https://doi.org/10.1016/j.cogsc.2022.100649.

(61) Smith, E. L.; Abbott, A. P.; Ryder, K. S. Deep Eutectic Solvents (DESs) and Their Applications. *Chem. Rev.* **2014**, *114* (21), 11060–11082. https://doi.org/10.1021/cr300162p.

(62) Chen, Y.; Liu, S.; Bi, Z.; Li, Z.; Zhou, F.; Shi, R.; Mu, T. Reviewing Electrochemical Stability of Ionic Liquids-/Deep Eutectic Solvents-Based Electrolytes in Lithium-Ion, Lithium-Metal and Post-Lithium-Ion Batteries for Green and Safe

Energy. *Green Energy Environ.* **2023**, S246802572300064X. https://doi.org/10.1016/j.gee.2023.05.002.

(63) Humphrey, W.; Dalke, A.; Schulten, K. VMD: Visual Molecular Dynamics. *J. Mol. Graph.* **1996**, *14* (1), 33–38. https://doi.org/10.1016/0263-7855(96)00018-5.

(64) Brehm, M.; Thomas, M.; Gehrke, S.; Kirchner, B. TRAVIS—A Free Analyzer for Trajectories from Molecular Simulation. *J. Chem. Phys.* **2020**, *152* (16), 164105. https://doi.org/10.1063/5.0005078.

(65) Hammond, O. S.; Bowron, D. T.; Edler, K. J. Liquid Structure of the Choline Chloride-Urea Deep Eutectic Solvent (Reline) from Neutron Diffraction and Atomistic Modelling. *Green Chem.* **2016**, *18* (9), 2736–2744. https://doi.org/10.1039/C5GC02914G.

(66) Malik, A.; Kashyap, H. K. Origin of Structural and Dynamic Heterogeneity in Thymol and Coumarin-Based Hydrophobic Deep Eutectic Solvents as Revealed by Molecular Dynamics. *Phys. Chem. Chem. Phys.* **2023**, *25* (29), 19693–19705. https://doi.org/10.1039/D3CP01770B.

(67) Kaur, S.; Gupta, A.; Kashyap, H. K. Nanoscale Spatial Heterogeneity in Deep Eutectic Solvents. *J. Phys. Chem. B* **2016**, *120* (27), 6712–6720. https://doi.org/10.1021/acs.jpcb.6b04187.

(68) Alizadeh, V.; Geller, D.; Malberg, F.; Sánchez, P. B.; Padua, A.; Kirchner, B. Strong Microheterogeneity in Novel Deep Eutectic Solvents. *ChemPhysChem* **2019**, *20* (14), 1786–1792. https://doi.org/10.1002/cphc.201900307.

(69) Cui, Y.; Kuroda, D. G. Evidence of Molecular Heterogeneities in Amide-Based Deep Eutectic Solvents. *J. Phys. Chem. A* **2018**, *122* (5), 1185–1193. https://doi.org/10.1021/acs.jpca.7b10264.

(70) Töpfer, K.; Pasti, A.; Das, A.; Salehi, S. M.; Vazquez-Salazar, L. I.; Rohrbach, D.; Feurer, T.; Hamm, P.; Meuwly, M. Structure, Organization, and Heterogeneity of Water-Containing Deep Eutectic Solvents. *J. Am. Chem. Soc.* **2022**, *144* (31), 14170–14180. https://doi.org/10.1021/jacs.2c04169.

(71) Shakiba, M.; Stippell, E.; Li, W.; Akimov, A. V. Nonadiabatic Molecular Dynamics with Extended Density Functional Tight-Binding: Application to Nanocrystals and Periodic Solids. *J. Chem. Theory Comput.* **2022**, *18* (9), 5157–5180. https://doi.org/10.1021/acs.jctc.2c00297.

(72) Srinivasan, H.; Sharma, V. K.; Sakai, V. G.; Mukhopadhyay, R.; Mitra, S. Noncanonical Relationship between Heterogeneity and the Stokes–Einstein Breakdown in Deep Eutectic Solvents. *J. Phys. Chem. Lett.* **2023**, *14* (43), 9766–9773. https://doi.org/10.1021/acs.jpclett.3c02132.

(73) Frenkel, D.; Smit, B. *Understanding Molecular Simulation: From Algorithms to Applications*, 2nd ed.; Computational science series; Academic Press: San Diego, 2002.

(74) Hug, S. Classical Molecular Dynamics in a Nutshell. In *Biomolecular Simulations*; Monticelli, L., Salonen, E., Eds.; Methods in Molecular Biology; Humana Press: Totowa, NJ, 2013; Vol. 924, pp 127–152. https://doi.org/10.1007/978-1-62703-017-5_6.

(75) Modern Methods and Algorithms of Quantum Chemistry. Proc: Proceedings; NIC series; NIC: Jülich, 2000.

(76) Vidossich, P.; De Vivo, M. The Role of First Principles Simulations in Studying (Bio)Catalytic Processes. *Chem Catal.* **2021**, *1* (1), 69–87. https://doi.org/10.1016/j.checat.2021.04.009.

(78) Thiel, W. Semiempirical Quantum–Chemical Methods. *WIREs Comput. Mol. Sci.* **2014**, *4* (2), 145–157. https://doi.org/10.1002/wcms.1161.

(79) Pople, J. A.; Segal, G. A. Approximate Self-Consistent Molecular Orbital Theory. III. CNDO Results for AB2 and AB3 Systems. *J. Chem. Phys.* **1966**, *44* (9), 3289–3296. https://doi.org/10.1063/1.1727227.

(80) Pople, J. A.; Beveridge, D. L.; Dobosh, P. A. Approximate Self-Consistent Molecular-Orbital Theory. V. Intermediate Neglect of Differential Overlap. *J. Chem. Phys.* **1967**, *47* (6), 2026–2033. https://doi.org/10.1063/1.1712233.

(81) Dewar, M. J. S.; Thiel, W. Ground States of Molecules. 38. The MNDO Method. Approximations and Parameters. *J. Am. Chem. Soc.* **1977**, *99* (15), 4899–4907. https://doi.org/10.1021/ja00457a004.

(82) Dewar, M. J. S.; Zoebisch, E. G.; Healy, E. F.; Stewart, J. J. P. Development and Use of Quantum Mechanical Molecular Models. 76. AM1: A New General Purpose Quantum Mechanical Molecular Model. *J. Am. Chem. Soc.* **1985**, *107* (13), 3902–3909. https://doi.org/10.1021/ja00299a024.

(83) Stewart, J. J. P. Optimization of Parameters for Semiempirical Methods I. Method. *J. Comput. Chem.* **1989**, *10* (2), 209–220. https://doi.org/10.1002/jcc.540100208.

(84) Stewart, J. J. P. MOPAC: A Semiempirical Molecular Orbital Program. *J. Comput. Aided Mol. Des.* **1990**, *4* (1), 1–103. https://doi.org/10.1007/BF00128336.

(85) Thiel, W.; Voityuk, A. A. Extension of the MNDO Formalism Tod Orbitals: Integral Approximations and Preliminary Numerical Results. *Theor. Chim. Acta* **1992**, *81* (6), 391–404. https://doi.org/10.1007/BF01134863.

(86) Thiel, W.; Voityuk, A. A. Extension of MNDO to d Orbitals: Parameters and Results for the Second-Row Elements and for the Zinc Group. *J. Phys. Chem.* **1996**, *100* (2), 616–626. https://doi.org/10.1021/jp952148o.

(10) Grimme, S.; Bannwarth, C.; Shushkov, P. A Robust and Accurate Tight-Binding Quantum Chemical Method for Structures, Vibrational Frequencies, and Noncovalent Interactions of Large Molecular Systems Parametrized for All Spd-Block Elements (*Z* = 1–86). *J. Chem. Theory Comput.* **2017**, *13* (5), 1989–2009. https://doi.org/10.1021/acs.jctc.7b00118.

(88) Seifert, G.; Joswig, J. Density-functional Tight Binding—an Approximate Density-functional Theory Method. *WIREs Comput. Mol. Sci.* **2012**, *2* (3), 456–465. https://doi.org/10.1002/wcms.1094.

(89) Elstner, M.; Porezag, D.; Jungnickel, G.; Elsner, J.; Haugk, M.; Frauenheim, Th.; Suhai, S.; Seifert, G. Self-Consistent-Charge Density-Functional Tight-Binding Method for Simulations of Complex Materials Properties. *Phys. Rev. B* **1998**, *58* (11), 7260–7268. https://doi.org/10.1103/PhysRevB.58.7260.

(90) Yang, Y.; Yu, H.; York, D.; Cui, Q.; Elstner, M. Extension of the Self-Consistent-Charge Density-Functional Tight-Binding Method: Third-Order Expansion of the Density Functional Theory Total Energy and Introduction of a Modified Effective Coulomb Interaction. *J. Phys. Chem. A* **2007**, *111* (42), 10861–10873. https://doi.org/10.1021/jp074167r.

(91) Bannwarth, C.; Caldeweyher, E.; Ehlert, S.; Hansen, A.; Pracht, P.; Seibert, J.; Spicher, S.; Grimme, S. Extended TIGHT-BINDING Quantum Chemistry Methods. *WIREs Comput. Mol. Sci.* **2021**, *11* (2), e1493. https://doi.org/10.1002/wcms.1493.

(92) Tolmachev, D.; Lukasheva, N.; Ramazanov, R.; Nazarychev, V.; Borzdun, N.; Volgin, I.; Andreeva, M.; Glova, A.; Melnikova, S.; Dobrovskiy, A.; Silber, S. A.; Larin, S.; De Souza, R. M.; Ribeiro, M. C. C.; Lyulin, S.; Karttunen, M. Computer Simulations of Deep Eutectic Solvents: Challenges, Solutions, and Perspectives. *Int. J. Mol. Sci.* **2022**, *23* (2), 645. https://doi.org/10.3390/ijms23020645.

(93) Klamt, A. Conductor-like Screening Model for Real Solvents: A New Approach to the Quantitative Calculation of Solvation Phenomena. *J. Phys. Chem.* **1995**, *99* (7), 2224–2235. https://doi.org/10.1021/j100007a062.

(94) Klamt, A.; Jonas, V.; Bürger, T.; Lohrenz, J. C. W. Refinement and Parametrization of COSMO-RS. *J. Phys. Chem. A* **1998**, *102* (26), 5074–5085. https://doi.org/10.1021/jp980017s.

(95) González De Castilla, A.; Bittner, J. P.; Müller, S.; Jakobtorweihen, S.; Smirnova, I. Thermodynamic and Transport Properties Modeling of Deep Eutectic Solvents: A Review on g^E -Models, Equations of State, and Molecular Dynamics. *J. Chem. Eng. Data* **2020**, *65* (3), 943–967. https://doi.org/10.1021/acs.jced.9b00548.

(96) Altamash, T.; Atilhan, M.; Aliyan, A.; Ullah, R.; García, G.; Aparicio, S. Insights into Choline Chloride–Phenylacetic Acid Deep Eutectic Solvent for CO_2 Absorption. *RSC Adv.* **2016**, *6* (110), 109201–109210. https://doi.org/10.1039/C6RA22312E.

(97) Altamash, T.; Nasser, M. S.; Elhamarnah, Y.; Magzoub, M.; Ullah, R.; Anaya, B.; Aparicio, S.; Atilhan, M. Gas Solubility and Rheological Behavior of Natural Deep Eutectic Solvents (NADES) via Combined Experimental and Molecular Simulation Techniques. *ChemistrySelect* **2017**, *2* (24), 7278–7295. https://doi.org/10.1002/slct.201701223.

(98) Gutiérrez, A.; Atilhan, M.; Aparicio, S. A Theoretical Study on Lidocaine Solubility in Deep Eutectic Solvents. *Phys. Chem. Chem. Phys.* **2018**, *20* (43), 27464–27473. https://doi.org/10.1039/C8CP05641B.

(99) Bedrov, D.; Piquemal, J.-P.; Borodin, O.; MacKerell, A. D.; Roux, B.; Schröder, C. Molecular Dynamics Simulations of Ionic Liquids and Electrolytes Using Polarizable Force Fields. *Chem. Rev.* **2019**, *119* (13), 7940–7995. https://doi.org/10.1021/acs.chemrev.8b00763.

(100) Doherty, B.; Acevedo, O. OPLS Force Field for Choline Chloride-Based Deep Eutectic Solvents. *J. Phys. Chem. B* **2018**, *122* (43), 9982–9993. https://doi.org/10.1021/acs.jpcb.8b06647.

(101) Abranches, D. O.; Coutinho, J. A. P. Everything You Wanted to Know about Deep Eutectic Solvents but Were Afraid to Be Told. *Annu. Rev. Chem. Biomol. Eng.* **2023**, *14* (1), 141–163. https://doi.org/10.1146/annurev-chembioeng-101121-085323.